Ore Geology Reviews 77 (2016) 1–24

Contents lists available at ScienceDirect

Ore Geology Reviews

journal homepage: www.elsevier.com/locate/oregeorev

Mineral chemistry and geochemical behavior of hydrothermal alterations associated with mafic intrusive-related Au deposits at the Atud area, Central Eastern Desert, Egypt

Amr Abdelnasser [a,b,*], Mustafa Kumral [a,**]

[a] Geological Engineering Department, Faculty of Mines, Istanbul Technical University, Istanbul, Turkey
[b] Geology Department, Faculty of Science, Benha University, Benha, Egypt

ARTICLE INFO

Article history:
Received 15 December 2015
Received in revised form 28 January 2016
Accepted 28 January 2016
Available online 30 January 2016

Keywords:
Hydrothermal alteration geochemistry
Mineral chemistry
Atud gold deposit
Egypt

ABSTRACT

Vein-type gold deposits in the Atud area are related to the metagabbro–diorite complex that occurred in Gabal Atud in the Central Eastern Desert of Egypt. This gold mineralization is located within quartz veins and intense hydrothermal alteration haloes along the NW–SE brittle–ductile shear zone, as well as along the contacts between them. By using the mass balance calculations, this work is to determine the mass/volume gains and losses of the chemical components during the hydrothermal alteration processes in the studied deposits. In addition, we report new data on the mineral chemistry of the alteration minerals to define the condition of the gold deposition and the mineralizing fluid based on the convenient geothermometers. Two generations of quartz veins include the mineralized grayish-to-white old vein (trending NW–SE), and the younger, non-mineralized milky white vein (trending NE–SW). The ore minerals associated with gold are essentially arsenopyrite and pyrite, with chalcopyrite, sphalerite, enargite, and goethite forming during three phases of mineralization; first, second (main ore), and third (supergene) phases. Three main hydrothermal alteration zones of mineral assemblages were identified (zones 1–3), placed around mineralized and non-mineralized quartz veins in the underground levels. The concentrations of Au, Ag, and Cu are different from zone to zone having 25–790 ppb, 0.7–69.6 ppm, and 6–93.8 ppm; 48.6–176.1 ppb, 0.9–12.3 ppm, and 39.6–118.2 ppm; and 53.9–155.4 ppb, 0.7–3.4 ppm, and 0.2–79 ppm for zones 1, 2, and 3, respectively.

The mass balance calculations and isocon diagrams (calculated using the GEOISO-Windows program) revealed the gold to be highly associated with the main mineralized zone as well as sericitization/kaolinitization and muscovitization in zone 1 more than in zones 2 and 3. The sericite had a higher muscovite component in all analyzed flakes (average $X_{Ms} = 0.89$), with 0.10%–0.55% phengite content in wall rocks and 0.13%–0.29% phengite content in mineralized quartz veins. Wall rocks had higher calcite ($CaCO_3$) contents and lower $MgCO_3$ and $FeCO_3$ contents than the quartz veins. The chlorite flakes in the altered wall rocks were composed of pycnochlorite and ripidolite, with estimated formation temperatures of 289–295 °C and 301–312 °C, respectively. Albite has higher albite content (95.08%–99.20%) which occurs with chlorite in zone 3.

© 2016 Elsevier B.V. All rights reserved.

1. Introduction

Mineralogical and bulk chemical changes reveal differences in the geochemical composition of hydrothermally altered and unaltered rocks. Reed (1997) stated that hydrothermal alteration processes refer to the physicochemical conditions in the hydrothermal system and ore precipitation results from the chemical interactions between rocks and hydrothermal solutions (Rose and Burt, 1979; Susak, 1994). These processes are typically associated with the gain and loss of components of the entire rock mass (Middelburg et al., 1988). Alteration zones regularly occur around mineralized veins and have definite fluid compositions based on the time and/or extent of interaction with the host rocks (Meyer and Hemley, 1967). The hydrothermal alteration zones around the ore and/or vein arrays are determined by the extent to which the original wall rocks were out of chemical equilibrium with the mineralizing fluids (Lindgren, 1894).

In the intrusion-related hydrothermal mineral systems, oxidized, I-type alkaline, and calc-alkaline magmas are considered to have a large capacity to carry and concentrate the base metals Au, Cu and Mo (Pirajno, 2009). The hydrothermal alteration minerals associated with intrusion-related gold deposits are formed during magmatic–hydrothermal processes by breakdown of host minerals by interaction with magmatic–hydrothermal fluids (Pirajno, 2009). In addition, the

* Correspondence to: Geological Engineering Department, Faculty of Mines, Istanbul Technical University, Istanbul, Turkey.
** Corresponding author.
E-mail addresses: amrkhalil@itu.edu.tr, abdelnasser82@gmail.com (A. Abdelnasser), kumral@itu.edu.tr (M. Kumral).

http://dx.doi.org/10.1016/j.oregeorev.2016.01.011
0169-1368/© 2016 Elsevier B.V. All rights reserved.

hydrothermal alteration associated with brittle–ductile shear zones suggests the presence of chemical ion exchange between wall rocks and hydrothermal fluids.

In Egypt, gold occurs in the Precambrian basement rocks of the Arabian-Nubian shield (ANS) that extends from the river Nile eastwards toward the Arabian Peninsula and southwards to the Mozambique Belt (Vail, 1988). Gold deposits are mainly confined to quartz-mineralized shear zones, which occur in the ophiolitic sequences, the island arc assemblages, the Hammamat and Dokhan Groups, and in the post-orogenic granitoids (El-Gaby et al., 1988; Pohl, 1988). Gold mineralization related to post-orogenic granitoids is very important as productive shear zones and quartz veins. Structurally, these shear zones were formed during compressional or transpressional late-stage events of the orogeny. Thus, the post-orogenic intrusions predated the quartz veins or shear zones and provided heat sources that resulted in the formation of hydrothermal convection cells. Interstitial waters dissolved available mineral species, and low concentrations of gold were derived from the strained rocks due to elevated temperature and pressure (Klemm et al., 2001).

The Atud gold deposit is located in the central part of the Egyptian Eastern Desert of Egypt (Fig. 1a) and represents one of the vein-type gold deposits in the ANS. Furthermore, this gold mineralization was largely distributed and controlled by two prominent fracture systems in the Eastern Desert of Egypt (Sabet and Bordonosov, 1984; Harraz and Ashmawy, 1994) and was closely associated with intense hydrothermal alteration haloes along the NW–SE brittle–ductile shear zone in the mined area (Harraz, 1999). El-Taher et al. (2003) determined the average concentration of gold in the Atud deposit to be 25.7 g/t using instrumental neutron activation analysis.

This paper focuses on the geochemical characteristics of least-altered host rock and hydrothermal alterations of the Atud gold deposit. We evaluated chemical exchanges between host rocks and hydrothermal fluids during hydrothermal alteration processes by applying mass/volume gains and losses of chemical components along with the mass balance calculations (Gresens, 1967; Grant, 1986, 2005; Middelburg et al., 1988; Leitch and Lentz, 1994). Electron microprobe analyses of alteration minerals were performed to determine the conditions of gold deposition and the mineralizing fluid according to the appropriate geothermometers.

2. Sampling and analytical methods

A total of 150 host rock, altered rock, and mineralized samples were collected during a number of field workings. Sixty thin-sections and polished sections were examined petrographically, and a subset were analyzed by scanning electron microscope (SEM) back-scattered electron imaging. Whole-rock (major and trace) and rare earth element analyses were conducted on 29 rock samples in the Geochemistry Research Laboratories of Istanbul Technical University (ITU/JAL). The samples were grounded using a Tungsten Carbide milling device. Major elements of the samples were analyzed using a BRUKER S8 TIGER model X-ray fluorescence spectrometer with a wavelength range from 0.01–12 nm. Trace elements were analyzed by Inductively Coupled Plasma-Mass Spectrometry using an ELAN DRC-e Perkin Elmer model. Approximately 50 mg of powdered sample was digested in two steps. The first step was completed with 6 ml of 37% HCl, 2 ml of 65% HNO_3 and 1 ml of 38–40% HF in a pressure- and temperature-controlled Teflon beaker using a Berghoff Microwave at 135 °C. The second step was

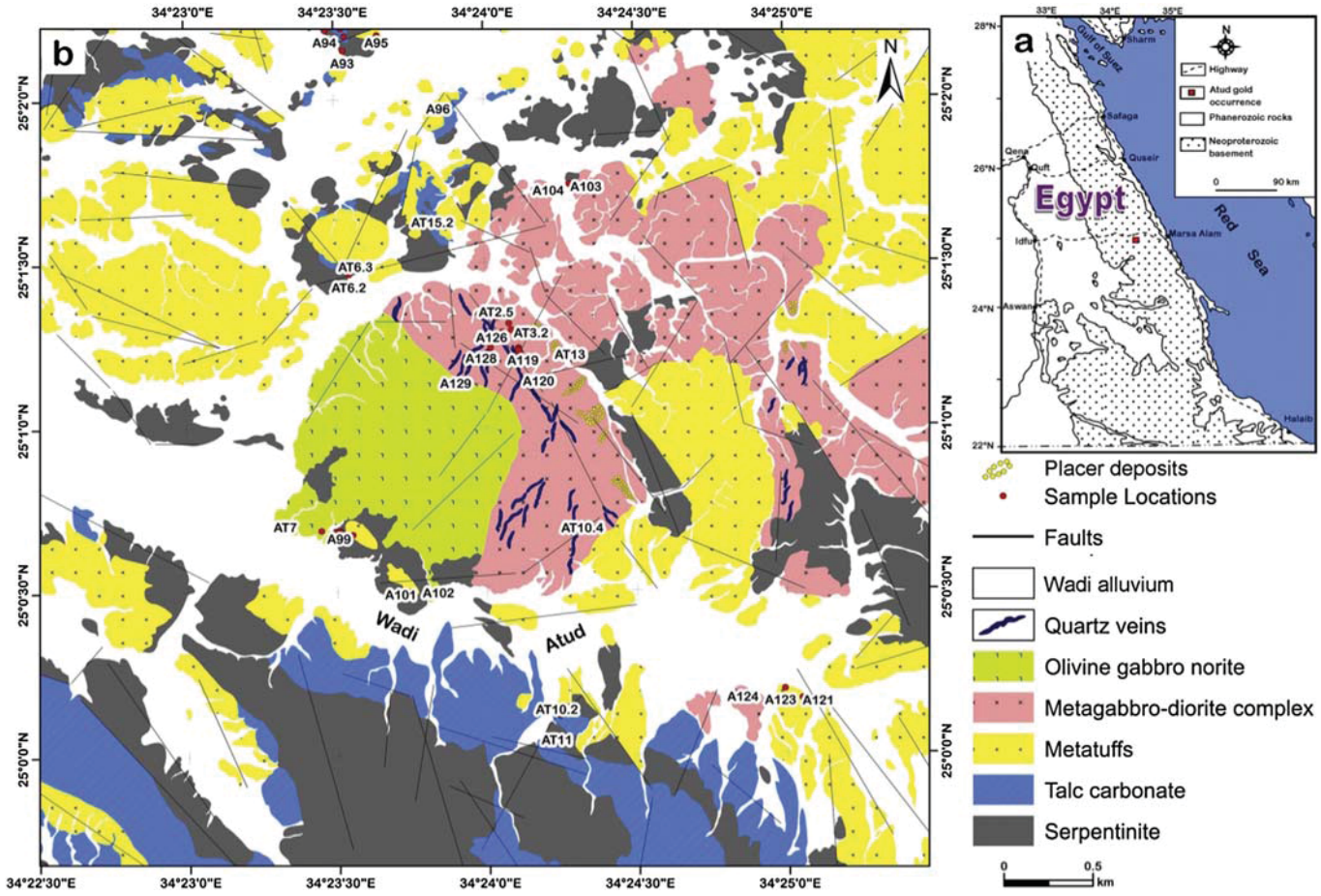

Fig. 1. a) Location map of Atud gold mine in the Central Eastern Desert of Egypt; b) Geologic map of the study area. Modified from Gabra (1986) and Harraz (1999).

completed with the addition of 6 ml of 5% boric acid solution. The altered rocks were also analyzed for mineralogy using a BRUKER X-ray diffractometer (XRD). Diagrams of rare earth elements were created using Igpet version 2.3 (Carr, 2007). Mass balance/volume changes were calculated and plotted using GEOISO-Windows (Coelho, 2006) by determining the absolute mobility of the elements using equations from Gresens (1967) and drawing isocon diagrams from Grant (1986, 2005). Mineral chemistry of hydrothermal minerals was performed by wavelength-dispersive X-ray spectrometry at TU-Clausthal, Germany, using a Cameca SX100 four spectrometer and a fully automated electron microprobe.

3. Geology of the study area

The Atud area is located at the extreme southern part of the Central Eastern Desert of Egypt (Fig. 1a). Atud lies within a region of low-grade metagabbro–diorite complex, ophiolitic rocks and a mélange of Neoproterozoic age and younger gabbro (Fig. 1b).

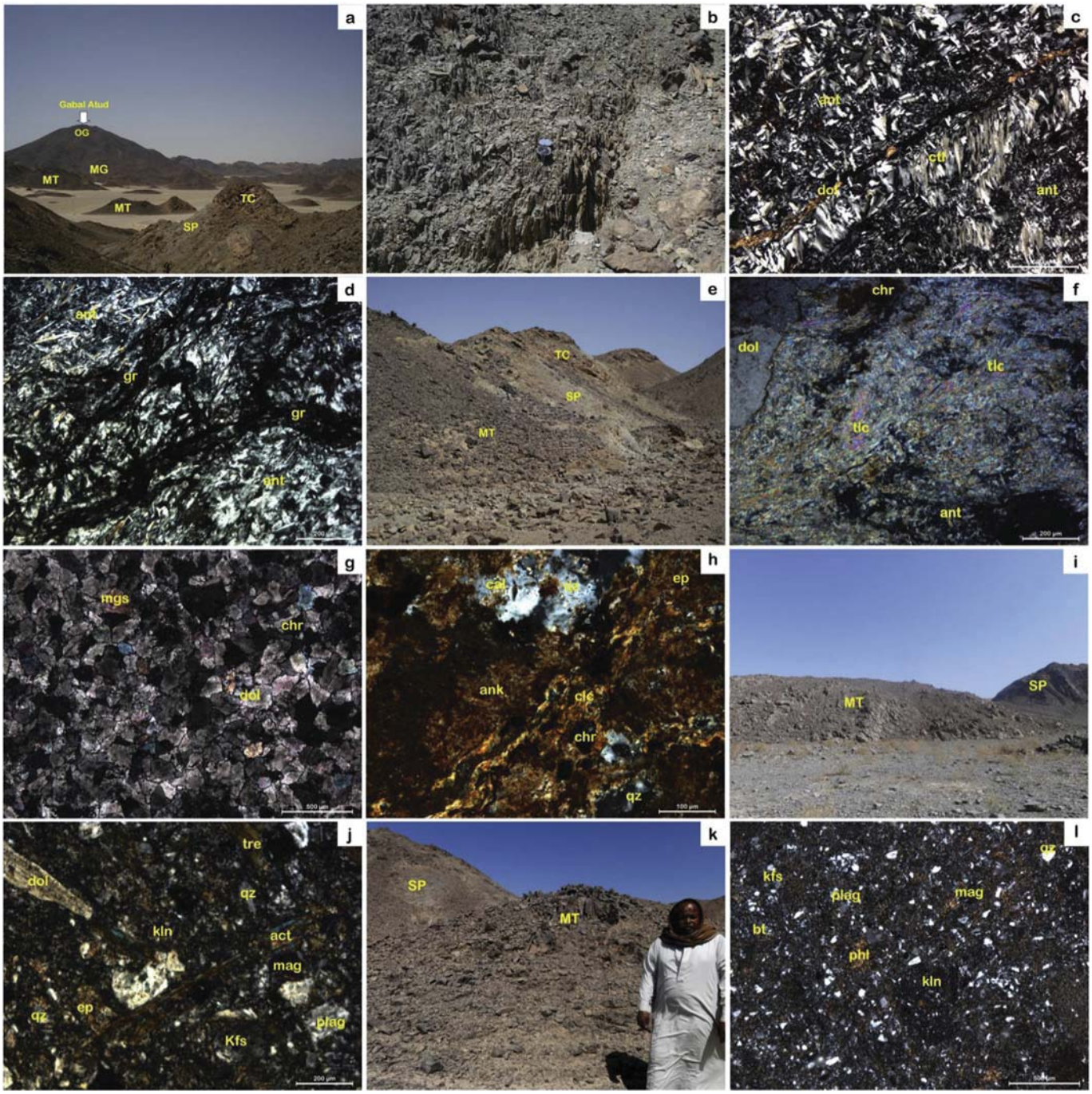

Fig. 2. a) Metagabbro–diorite complex (MG) of Gabal Atud intruded into country rocks and latterly intruded by olivine gabbro (OG); b) deformation and shearing in serpentinite rocks (SP); c) photomicrograph shows the mineral compositions of serpentinite rocks; d) Graphite (gr) with antigorite (ant) in serpentinite rocks; e) talc–carbonate rocks (TC) are associated with serpentinite rocks (SP) and metatuffs (MT); f) talc (tlc) with dolomite (dol) and antigorite (ant) in talc–carbonate rocks; g) dolomite (dol) with subordinate amounts of magnesite (mgs) and chromite (chr) in dolomitic marble; h) mineral compositions of calc–silicate rocks; i) basic lapilli metatuffs (MT) thrust over the serpentinites (SP) at Wadi Atud; j) mineral compositions of basic lapilli metatuffs; k) intermediate metatuffs (MT) occur serpentinite rocks (SP) at the northern part of the study area; l) kaolinitized microperthite (kfs), biotite (bt), phlogopite (pht), and quartz (qz) represent the main constituents of intermediate metatuffs.

A detailed field study revealed that the study area covers 18 km^2 and is composed mainly of metagabbro–diorite complex emplaced into serpentinites and their derivatives and metatuffs (Fig. 1b). This complex is later intruded by olivine gabbro norite rocks. The Atud gold deposit area is traversed by many quartz veins and dykes of different compositions and directions, which are concentrated in the eastern, northeastern and southeastern parts of the area (Fig. 1b). Structurally, the Atud area was affected by brittle–ductile shear zone that showed in altered metagabbro–diorite rocks trending in the NW–SE direction (Fig. 1b).

The serpentinites and their derivatives represent the Pan-African dismembered ophiolitic rocks exposed in the Atud area. These rocks occupy a large area which is distributed around Gabal Atud (Figs. 1b & 2a). The rocks are geologically and petrographically differentiated into serpentinite, talc-carbonate, dolomitic marble, and calc-silicate rocks. Serpentinite rocks are highly deformed and shearing; their foliation directions are N 60 W dipping 70° toward SW (Fig. 2b). The serpentinites are composed of antigorite and chrysotile, with minor amounts of tremolite, actinolite, dolomite, and chromite (Fig. 2c). They are also rich in graphite in the northern part of the study area, that occurred along with the talc serpentinite and the calc silicate rocks (Fig. 2d). Talc-carbonate rocks are exposed at the southern part of the study area, and are closely associated with serpentinite rocks

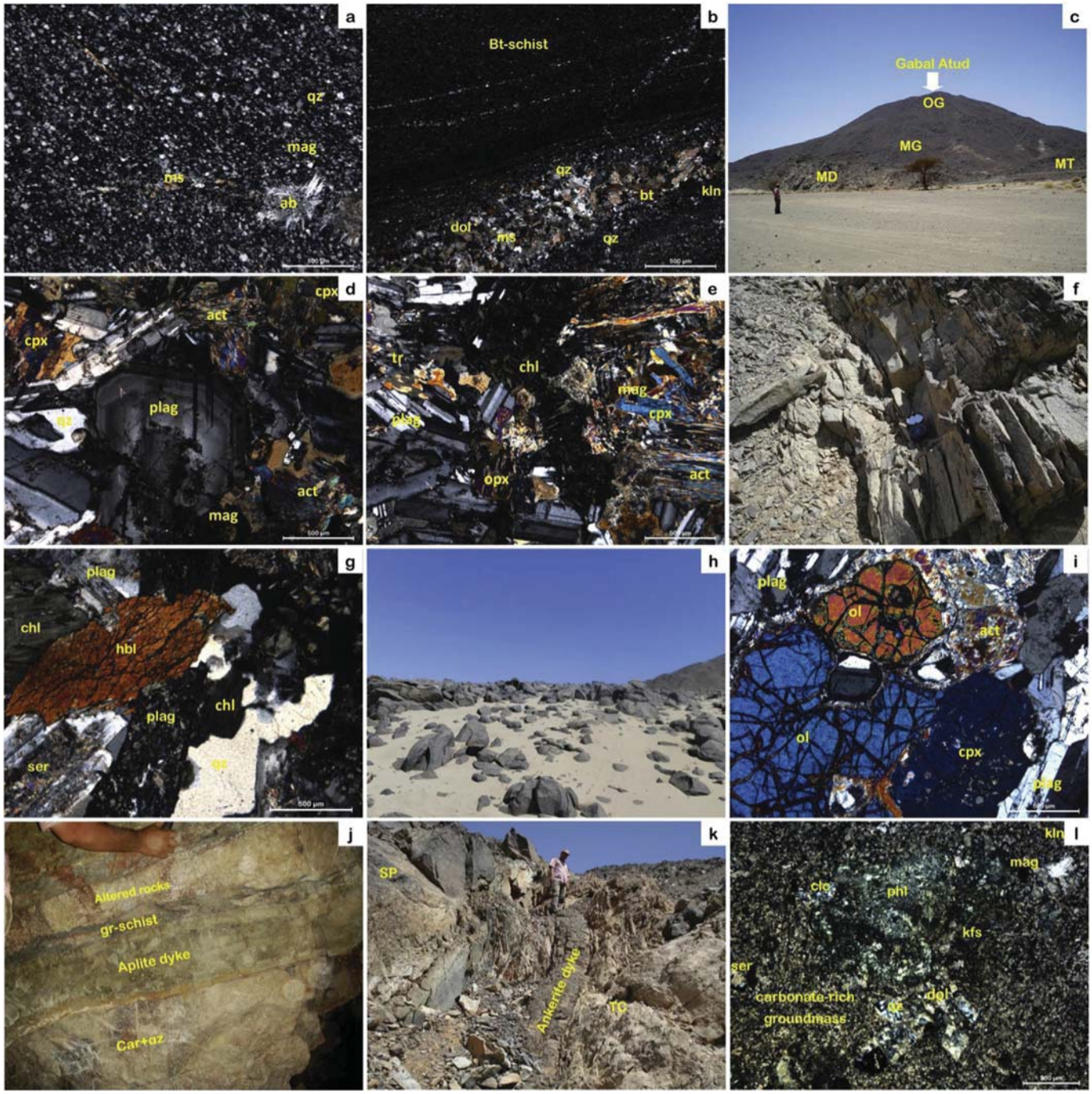

Fig. 3. a); b) Photomicrographs of metachert and quartz biotite schist, respectively; c) metagabbro–diorite complex represents the main body of Gabal Atud; d), e) plagioclase (plag), actinolite (act), and tremolite (tr) with quartz (qz), chlorite (chl), clinopyroxene (cpx), orthopyroxene (opx) in the metagabbros (MG); f) diorite is affected by shearing; g) photomicrograph of dioritic rocks; h) boulder weathering of olivine gabbro norite (OG); i) olivine (ol) with plagioclase (plag), clinopyroxene (cpx), and orthopyroxene (opx) in olivine gabbro norite; j) aplitic dyke cut through the metagabbro-dioritic rocks at Gabal Atud; k) ankeritic dyke cut through the serpentinite rocks (SP) at the northern part of the study area; l) mineral compositions of aplite dyke.

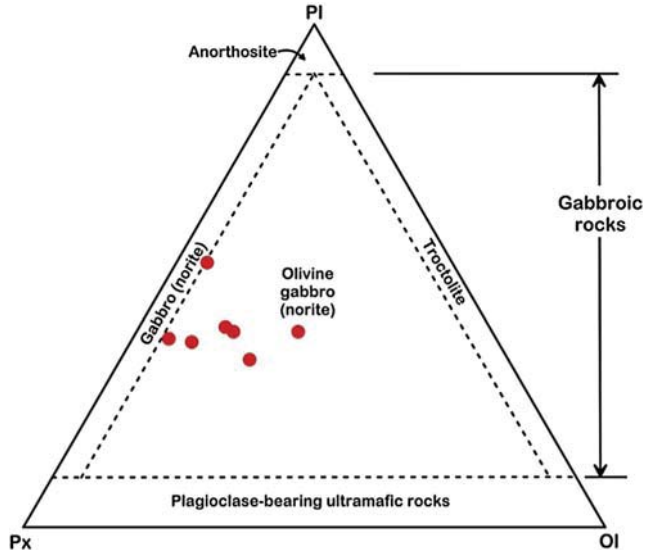

Fig. 4. Modal mineralogy of olivine gabbro norite, Streckeisen (1976), Pl = plagioclase; Px = pyroxene; Ol = olivine.

and metatuffs (Figs. 1b and 2e). These rocks are mainly composed of talc (45–55 vol.%) and carbonate (dolomite; 40–50 vol.%), with minor amount of antigorite, actinolite, and chromite (Fig. 2f). Dolomitic marble is exposed only in the southern slope of Gabal Atud, occurring as small isolated masses of dark grayish medium-to-fine-grained rocks (Fig. 1b). The marble consists essentially of dolomite (90 vol.%) with subordinate amounts of magnesite and chromite (Fig. 2g). Calc-silicate rocks occur at the northern part of the study area and are composed essentially of ankerite, dolomite, and quartz, with minor amounts of calcite, clinochlore, epidote, and chromite (Fig. 2h).

Metatuffs are exposed associated with serpentinite rocks and form low-lying outcrops distributed around Gabal Atud (Figs. 1b and 2a). Metatuffs are microscopically differentiated into different varieties; mafic lapilli metatuffs, intermediate metatuffs, metacherts, and quartz biotite schists. All are slightly layered, and were subjected to low-grade metamorphism within the greenschist facies. Mafic lapilli metatuffs are exposed as an elongate body trending NW–SE and thrust over the serpentinites at the southern part of the study area, at Wadi Atud (Fig. 2i). These metatuffs are fine-grained dark gray-to-greenish gray in color and are composed of carbonatized plagioclase with actinolite, tremolite, epidote, and dolomite set in a microcrystalline tuffaceous matrix of microcrystalline aggregates of kaolinitized feldspar, tremolite–actinolite, zoisite, quartz, and dusty iron oxide (Fig. 2j).

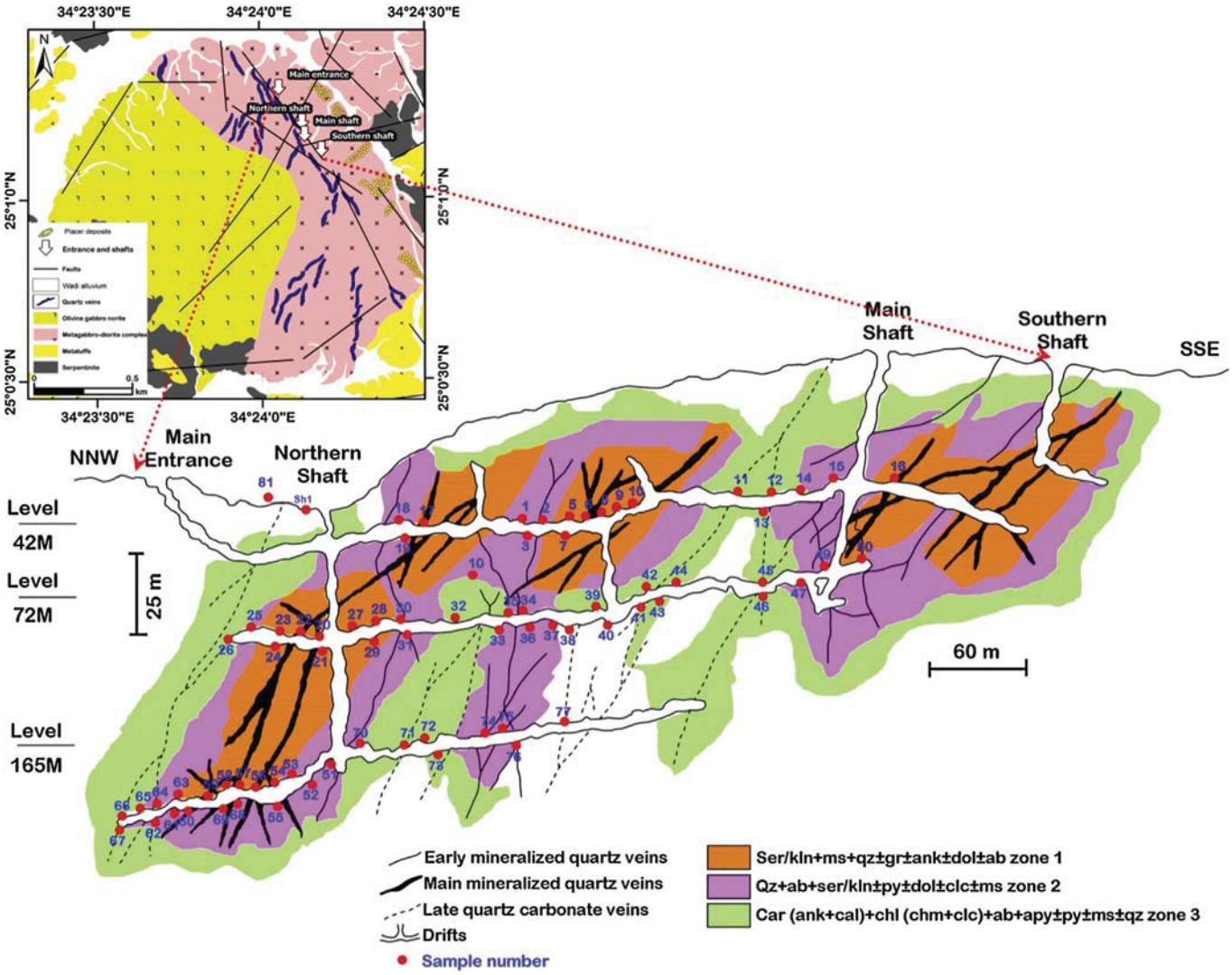

Fig. 5. Longitudinal section shows drifting of underground working of the Atud gold mine (traced quartz vein stages and alteration zones, after Gabra, 1986; Harraz, 1999).

Table 1
Description of three levels of the underground working of main Atud deposits.

	1st level	2nd level	3rd level
Depth	~40 m	~70 m	~160 m
Alteration	–Sericitization –Carbonation (ankerite) –Argillic	–Sericitization –Carbonation (ankerite & calcite) –Silicification –Agillic –Sulfidation	–Sericitization –Agillic (kaolinite) –Carbonation (ankerite & calcite)
Quartz veins	–Mostly gray quartz (N20W/45W) with variable amount of milky quartz (N30W/50SW) and very little of smoky quartz.	–Mostly milky quartz and gray quartz with laminated quartz (N40W/50 W).	–Mostly milky quartz with gray quartz (N40W/50SW) and laminated quartz.
Deformation	–N–S/55 W. –N 40 W/70 NE. –N 20 W/60 NE. –N 20 E/10 SE.	–N–S/55 W.	–N 25 W/50 SW.

Intermediate metatuffs, which occur at the northern part of the study area with serpentinite rocks (Fig. 2k), are composed of kaolinitized microperthite, biotite, plagopite, and quartz with minor amounts of plagioclase and iron oxide in a much finer tuffaceous matrix of microcrystalline aggregates of kaolinitized feldspar, quartz, biotite and dusty iron oxide (Fig. 2l). Metacherts occupy a small area on the southern slope of Gabal Atud, interposed with serpentinite rock. They are slightly laminated, consisting of irregularly banded quartz- and feldspar-containing laminae containing muscovite, carbonate, and iron oxide (Fig. 3a). Quartz biotite schists, which form low-lying foliated outcrops, are composed mainly of quartz and feldspar with biotite and subordinate muscovite, carbonate, and opaque minerals (Fig. 3b).

The metagabbro–diorite complex forms the main part of Gabal Atud, occurring as a semicircular body, and has an obvious intrusive contact

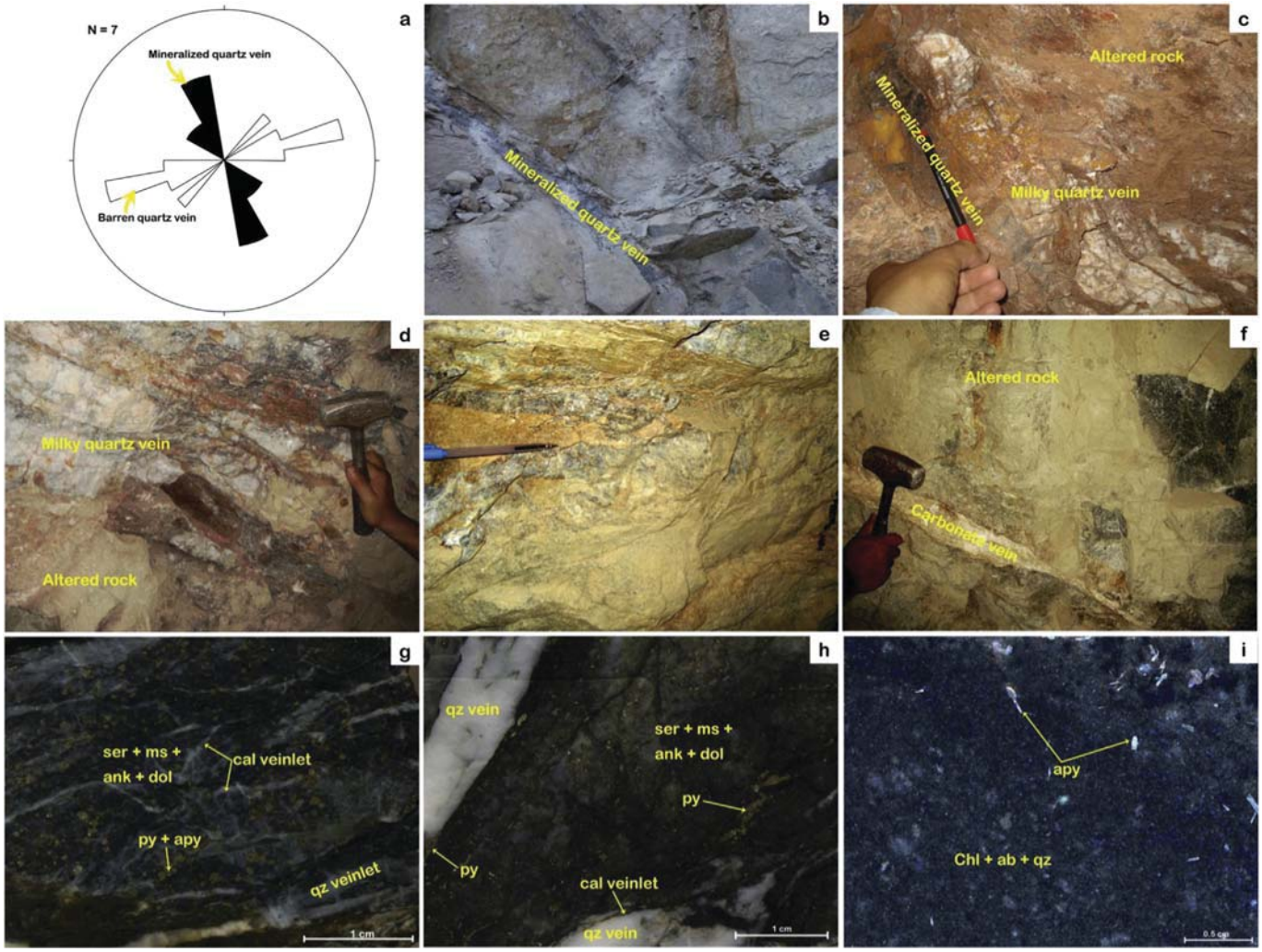

Fig. 6. a) Rose diagram showing for two type of quartz veins; b) mineralized gray quartz vein cut through altered rocks; c) gray quartz vein with variable amounts of milky one in the first underground level (42 m depth); d) milky quartz veins mainly placed in the second underground level (72 m depth); e) pinching, swelling and bifurcation into small veins and veinlets in level 2, f) carbonate veinlets cut through the third underground level (165 m depth) with milky quartz; g) high amount of pyrite (py) and arsenopyrite (apy) within the alteration minerals in zone 1; h) milky quartz vein and calcite (cal) veinlets cut through the wall rocks at sulfidized zone 2; i) reflected light centimeter-scale view of chloritization (chl), albitization (ab), and silicification (qz) with arsenopyrite (apy) in zone 3.

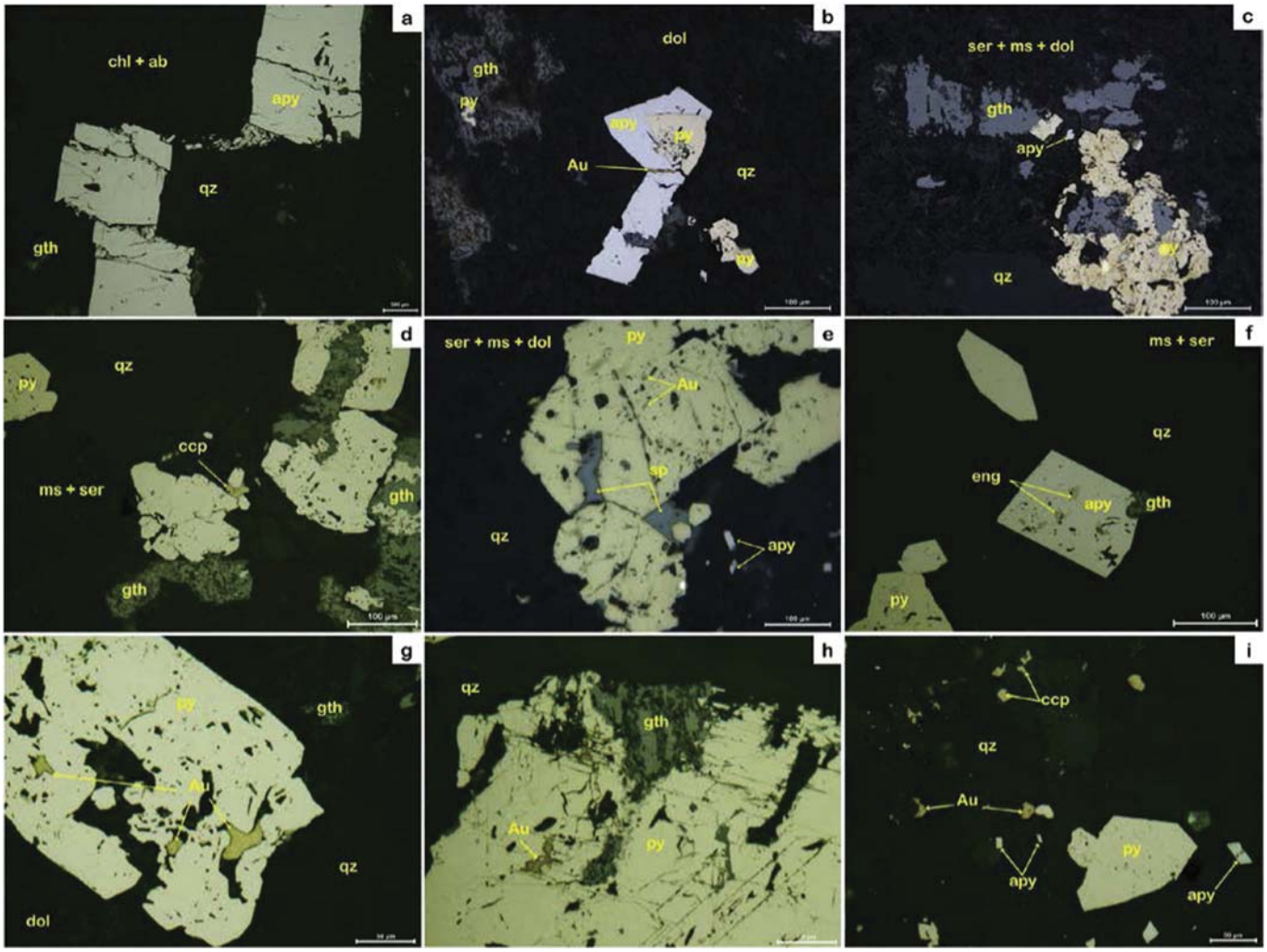

Fig. 7. Photomicrographs of reflected light microscopy: a) Deformed arsenopyrite (apy) in the altered rocks; b) gold (Au) filled the cracks in arsenopyrite (apy) that associated with pyrite (py); c) pyrite (py) with arsenopyrite (apy) and goethite (goe); d) chalcopyrite (ccp) associated with pyrite (py); e) inclusions of sphalerite (sp) in the large pyrite (py); f) enargite (eng) occurred as inclusion in arsenopyrite grains (apy); g) microfractures of pyrite (py) filled by gold (Au); h) inclusions of gold (Au) in pyrite crystals (py); i) gold (Au) occurred as disseminated grains with chalcopyrite (ccp) and pyrite (py) in the alteration zones.

against serpentinites and metatuffs (Figs. 1b and 2a–3c). This complex is one of the early orogenic gabbro–diorite complexes in the Egyptian part of the Nubian shield, with an age ranging from 987 Ma to 830 Ma (Hashad, 2013; Abdel-Rahman and Doig, 1987). It was invaded by olivine gabbro norite of group III of Ghoneim (1989). At the study area, this complex consists of metamorphosed gabbros and diorite, with quartzo-

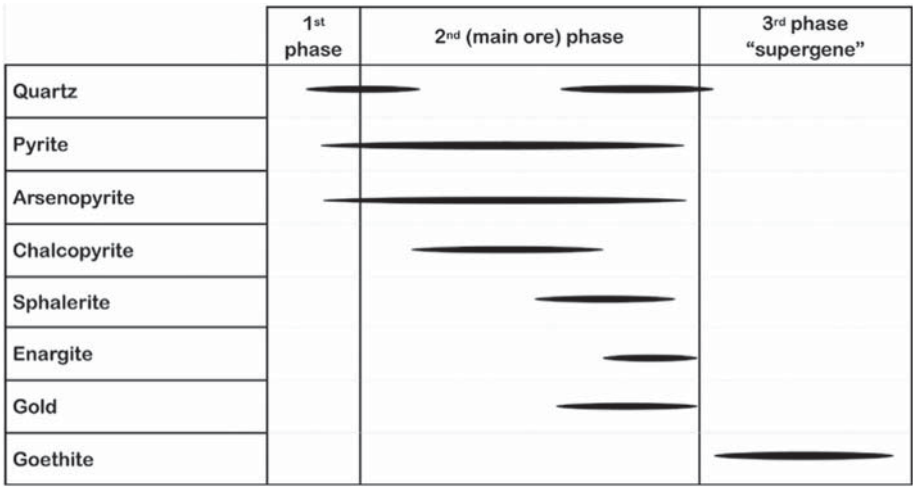

Fig. 8. Paragenetic sequence of quartz, sulfide minerals, and supergene minerals as defined by mineral assemblages.

feldspathic veined hybrid leucocratic metagabbros between them (Fig. 3c). The complex, which is affected by many types of alterations, represents the main host rocks of the gold-bearing quartz veins occurring along the shear zone trending NW–SE at the eastern and southeastern slopes of Gabal Atud (Fig. 1b). The metagabbros are medium-to-coarse-grained and have hypidiomorphic granular textures with poikilitic or ophitic-to-subophitic textures composed of plagioclase, actinolite, and tremolite together with variable amounts of secondary quartz, chlorite, clinopyroxene, orthopyroxene, and opaque minerals (hematitic iron oxides) (Fig. 3d-e). Plagioclase is labradorite in composition (An_{50-65}), zoned (Fig. 2d), and affected by sericitization, kaolinitization, and carbonatization (Fig. 3e). In contrast, the diorite is affected by shearing (Fig. 2f) and is composed essentially of altered plagioclase and hornblende with minor amounts of quartz, tremolite–actinolite, chlorite and iron oxide (Fig. 3g).

Olivine gabbro–norites are non-deformed rocks equivalent to younger gabbro of group III of Ghoneim (1989), that intrude into the metagabbro–diorite complex of Gabal Atud (Figs. 1b and 3a). Therefore, these rocks have intrusive contact with the metagabbro diorite complex and are different from it because they have very little and/or no alteration relative to the metagabbro–diorite complex that represent the host rocks of Atud gold deposit which are typically altered. In addition,

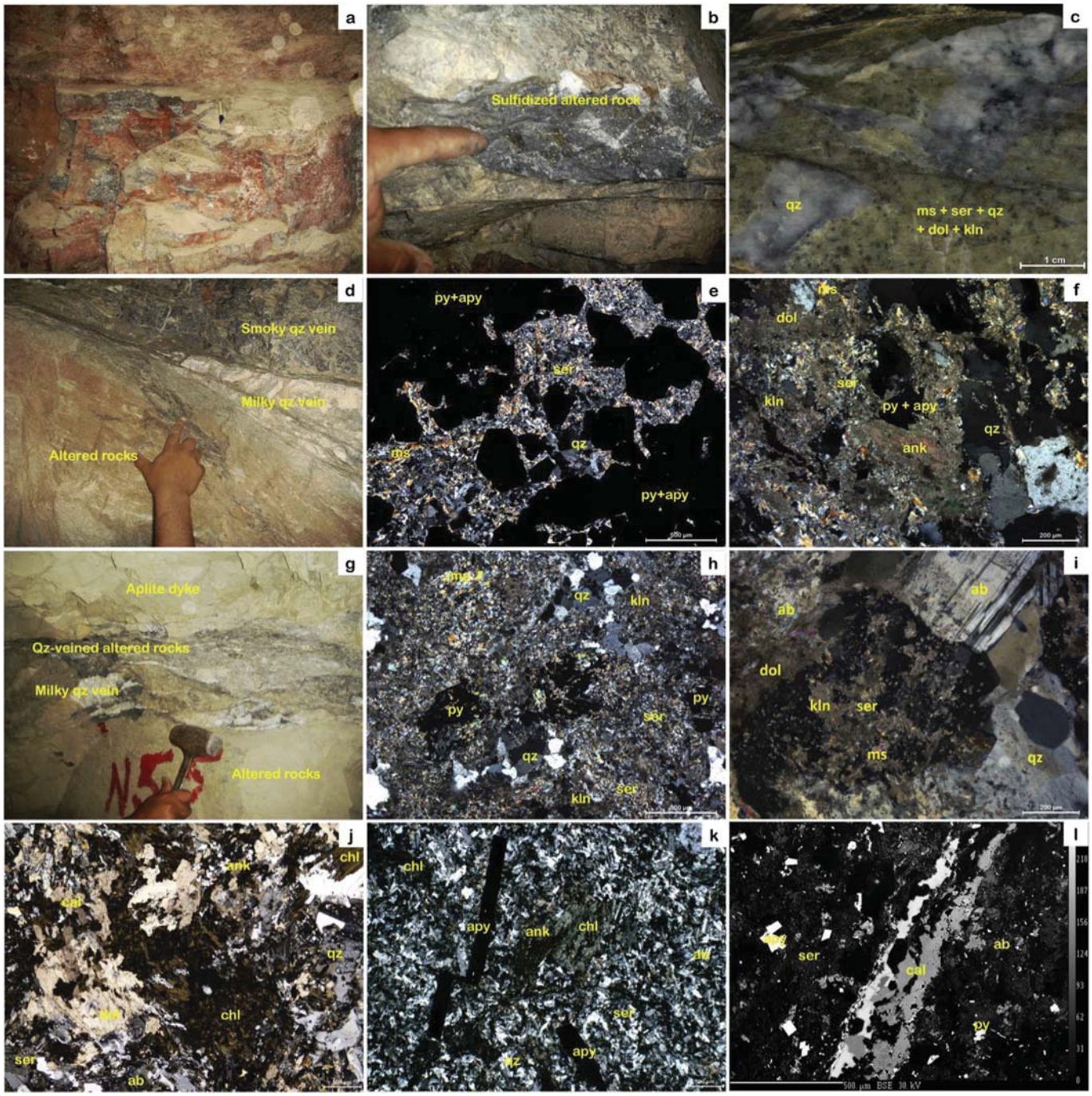

Fig. 9. a) Main mineralized quartz (qz) in veins grayish/reddish wall rocks of zone 1 affected by faulting; b) highly sulfidized wall rocks in zone 1; c) gray quartz (qz) vein cut through wall rocks; d) variable amounts of milky and smoky quartz veins in zone 1; e), f) photomicrographs show the alteration products at zone 1; g) milky quartz vein (qz) and calcite veinlets cut through the wall rocks at sulfidized zone 2; h), i) quartz (qz), albite (ab), and sericite (ser)/kaolinite (kln) with pyrite (py), dolomite (dol), clinochlore (clc), and muscovite (ms) in zone 2; j); k) photomicrographs show the alteration products with arsenopyrite (apy) in zone 3; l) backscattered images of the calcite (cal), quartz (qz), and albite (ab) with sericite (ser) in zone 3.

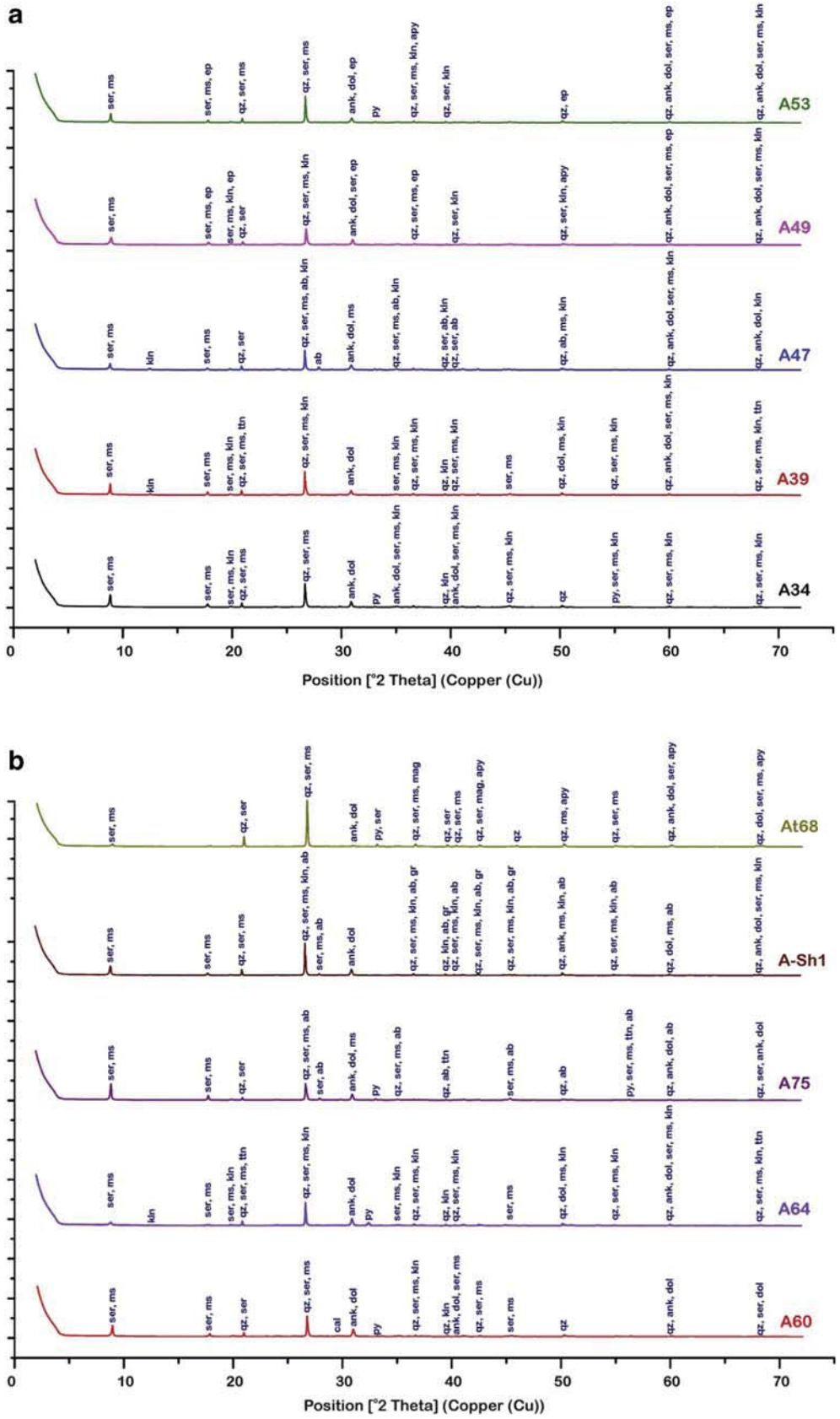

Fig. 10. XRD patterns of altered samples collected from the different alteration zones: a), b) zone 1; c) zone 2; d) zone 3. Abbreviation: ankerite (ank), anorthite (an), anthophyllite (ath), arsenopyrite (apy), calcite (cal), chamosite (chm), chlorite (chl), clinochlore (clc), dolomite (dol), epidote (ep), graphite (gr), kaolinite (kln), magnetite (mag), muscovite (ms), orthoclase (or), pyrite (py), quartz (qz), sericite (ser), titanite (ttn), tremolite (tr), zeolite (zeo).

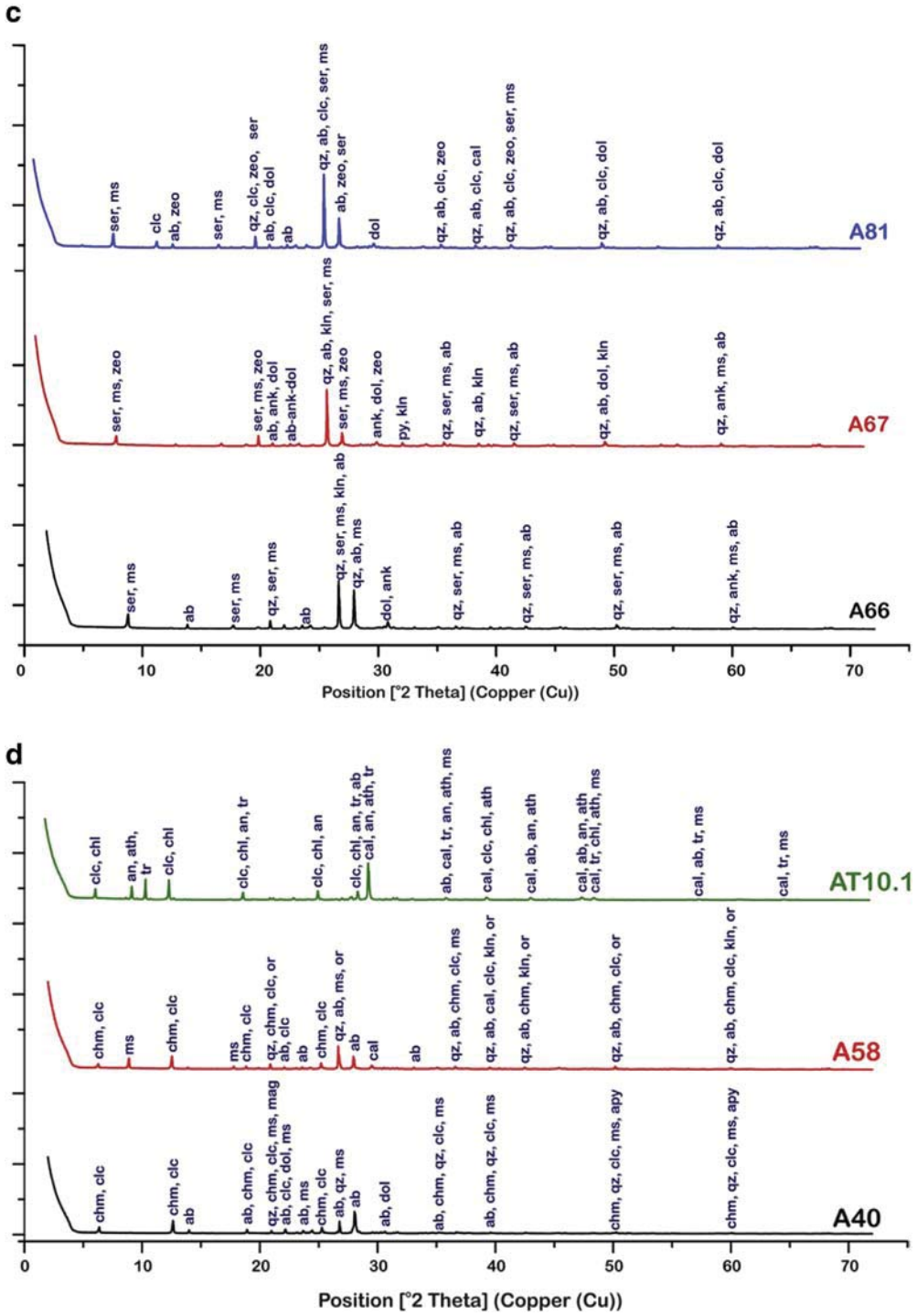

Fig. 10 (*continued*).

they are massive, dark gray and coarse-to-medium-grained, with no signs of mineral foliation and no evidence of ductile and/or brittle deformation, emphasizing the rocks' post-tectonic emplacement. They also show as small boulders along the western slope of Gabal Atud (Fig. 3h). They consist mainly of plagioclase (labradorite to bytownite; 35–40 vol.%), hypersthene (15–20 vol.%), diopside (25–30 vol.%) partially altered to tremolite–actinolite (~5 vol.%), cumulate olivine (partly altered into serpentine minerals, 15–20 vol.%) and opaque minerals (~3 vol.%) (Fig. 3i). Based on modal mineralogical studies, these rocks are olivine gabbro norite (Fig. 4).

Dykes, in the study area, trend mostly in the NW–SE direction. Porphyritic andesite and aplitic dykes (trending N 40 W dipping at 50° toward SW) cut through the metagabbro-dioritic rocks at Gabal Atud (Fig. 3j), but few dykes run roughly NNE–SSW except for an ankerite dyke which is the oldest one and cuts through the serpentinite rocks at the northern part of the study area (Fig. 3k). The samples of the aplite dyke are yellowish, fine-grained rocks with porphyritic textures composed mainly of phenocrysts of carbonatized plagioclase, biotite and/or phlogopite (partly altered to chlorite) in a carbonate-rich groundmass with potassium feldspar, quartz, sericite, and iron oxide (Fig. 3l).

Table 2
Major, trace, and rare earth elements (REE) of metagabbro–diorite complex at Atud area.

	Metagabbro							Diorite			
Sample ID	A 42	A105	A124	A96	A124	A128	AT10.4	A14	A 103	A115	A116
SiO_2	53.11	49.87	54.13	49.67	54.13	45.24	45.68	57.77	53.10	54.00	55.80
Al_2O_3	15.81	16.19	16.79	13.79	16.79	13.96	16.72	16.69	18.33	15.79	16.37
Fe_2O_3	7.83	8.53	7.73	9.00	7.73	6.47	7.05	6.71	7.39	7.43	6.24
MgO	6.94	8.19	3.86	9.43	3.86	11.26	10.45	3.16	5.58	6.34	5.25
CaO	6.99	10.26	5.16	8.57	5.16	15.69	15.09	6.59	8.66	7.18	6.40
Na_2O	2.62	2.43	3.10	2.93	3.10	1.46	1.37	4.39	3.10	2.84	3.53
K_2O	0.74	0.36	2.05	0.76	2.05	0.20	0.14	0.93	0.37	0.67	0.83
TiO_2	0.74	0.65	1.23	1.00	1.23	0.45	0.48	0.92	0.98	0.71	0.63
P_2O_5	0.13	0.11	0.38	0.35	0.38	0.06	0.06	0.26	0.18	0.12	0.11
MnO	0.14	0.14	0.11	0.16	0.11	0.12	0.13	0.11	0.13	0.13	0.11
Cr_2O_3		0.05	0.01	0.09	0.01	0.17	0.05	0.01			
LOI	3.99	3.23	5.45	4.26	5.45	4.91	2.28	2.45	2.28	3.66	3.78
Trace and rare earth elements (ppm)											
Ag	0.9	0.8	1.4	1.1	1.4	0.6	0.3	0.7	0.3	0.8	1.1
As	16.0	3.0	1.0	7.0	1.0	9.0	33.0	8.0	3.0	26.0	10.0
Au (ppb)	35.9	156.2	22.2	27.2	22.2	69.6	8.4	75.1	16.9	49.5	27.7
Ba	167.0	113.0	43.0	131.0	43.0	26.0	41.5	208.0	126.0	160.0	194.0
Be	1.2	1.2	1.8	1.5	1.8	0.9	0.5	1.4	0.7	1.4	1.3
C	349.9	1647.1	6602.0	2461.8	6602.0	3620.0	1096.6	2543.7	100.7	323.2	399.5
Cd	0.4	0.3	0.5	0.7	0.5	0.3	4.0	0.2	0.2	0.6	0.6
Co	31.0	50.0	28.0	44.0	28.0	36.0	45.2	42.0	24.0	31.0	26.0
Cr	0.0	329.8	95.8	604.1	95.8	1132.4		93.7	0.0	0.0	0.0
Cs	32.0	0.3	0.4	0.3	0.4	0.4	0.0	0.9	0.1	0.6	1.3
Cu	15.1	21.8	72.1	22.3	72.1	28.8	12.7	18.5	15.8	22.6	19.5
Ga	0.7	30.9	62.4	32.2	62.4	15.4	10.0	40.8	15.9	33.4	38.4
Hf	1.6	0.8	5.9	3.1	5.9	0.9	0.9	1.2	3.1	2.6	1.2
In	0.1	0.1	0.1	0.1	0.1	0.0	0.0	0.1	0.0	0.1	0.1
Ir	0.0	0.2	0.0	0.0	0.0	0.0	0.0	0.1	0.0	0.0	0.0
Li	10.0	8.6	15.3	12.6	15.3	4.8	4.8	12.2	3.0	9.4	10.1
Ni	42.0	237.4	240.0	352.5	240.0	224.1	34.5	209.3	23.0	31.0	22.0
Pb	3.6	8.1	25.4	16.3	25.4	14.9	21.0	15.8	0.2	3.9	4.8
Pd	1.0	0.7	5.4	2.7	5.4	0.8	1.1	0.9	1.2	0.8	0.8
Pt	0.0	0.0	0.0	0.0	0.0	0.0	0.0	0.0	0.0	0.0	0.0
Rb	29.5	15.0	39.8	19.0	39.8	10.7	1.8	36.5	11.0	60.0	27.0
Rh	0.1	0.1	0.1	0.1	0.1	0.1	0.1	0.1	0.1	0.1	0.1
Ru	0.1	0.2	0.1	0.1	0.1	0.2	0.0	0.1	0.1	0.1	0.2
S	250.0	132.1	99.4	208.2	99.4	104.5	1398.3	235.8	244.3	656.9	213.5
Sb	0.8	4.1	4.6	8.8	4.6	7.9	0.2	5.5	0.5	0.7	1.1
Sn	1.7	1.3	2.9	1.8	2.9	1.6	0.8	2.0	1.7	1.6	1.5
Sr	436.2	362.9	366.0	347.1	366.0	336.5	229.7	454.2	334.0	317.0	443.9
Te		–	–	–	–	0.0	0.0	–	–	–	–
Tl	0.1	0.0	0.1	0.1	0.1	0.0	0.0	0.1	0.0	0.1	0.1
U	0.5	0.2	1.2	0.7	1.2	0.2	0.3	0.5	0.1	0.4	0.4
V	369.7	510.4	486.7	577.6	486.7	443.8		344.4	417.1	442.1	389.4
Zn	101.9	109.7	141.1	189.4	141.1	84.8	20.8	134.6	51.1	105.6	109.2
Zr	80.0	47.0	202.0	115.0	202.0	42.0	73.0	107.0	105.0	86.0	96.0
Sc	245.6	234.4	216.5	220.0	216.5	275.7	123.7	221.5	217.7	213.2	206.5
Y	29.1	22.0	58.0	31.6	58.0	17.0	9.6	36.0	37.5	29.4	24.6
La	11.3	5.5	28.4	25.7	28.4	3.4	2.2	15.0	14.3	11.7	11.0
Ce	25.6	12.9	67.2	58.7	67.2	8.6	5.7	34.0	32.8	26.5	23.3
Pr	3.3	1.8	8.5	7.2	8.5	1.3	0.8	4.4	4.4	3.5	3.0
Nd	15.4	8.9	37.4	30.8	37.4	6.5	3.9	20.7	20.4	15.7	13.6
Sm	6.1	2.6	9.4	6.5	9.4	2.0	1.3	5.5	5.2	4.1	3.5
Eu	3.1	1.4	2.4	2.0	2.4	0.8	0.6	2.1	1.8	1.5	1.4
Gd	4.8	3.3	10.1	6.7	10.1	2.7	1.7	6.2	6.1	4.7	4.0
Tb	0.7	0.5	1.5	0.9	1.5	0.4	0.3	0.9	0.9	0.7	0.6
Dy	4.7	3.4	9.1	5.4	9.1	2.8	1.8	5.7	5.9	4.7	3.9
Ho	1.0	0.7	1.8	1.1	1.8	0.6	0.4	1.2	1.2	0.9	0.8
Er	2.9	2.1	5.4	3.1	5.4	1.6	1.0	3.5	3.6	2.8	2.3
Tm	0.4	0.3	0.7	0.4	0.7	0.2	0.1	0.5	0.5	0.4	0.3
Yb	2.7	2.0	4.6	2.7	4.6	1.4	0.9	3.0	3.1	2.6	2.1
Lu	0.5	0.3	0.7	0.4	0.7	0.2	0.1	0.4	0.5	0.4	0.3
Th	2.1	3.4	5.6	4.0	5.6	0.5	0.3	2.5	1.9	2.1	2.3
Parameters											
FeO*	7.5	8.0	7.4	8.5	7.4	6.2	6.6	6.2	6.8	7.1	5.9
$Na_2O + K_2O$	3.4	2.8	5.1	3.7	5.1	1.7	1.5	5.3	3.5	3.5	4.4
FeO*/MgO	1.1	1.0	1.9	0.9	1.9	0.5	0.6	2.0	1.2	1.1	1.1
Zr/Y	2.7	2.1	3.5	3.6	3.5	2.5	7.6	3.0	2.8	2.9	3.9
Σ REE	82.4	45.9	187.2	151.6	187.2	32.4	20.8	103.1	100.7	80.1	70.2
Σ LREE	64.8	33.1	153.3	130.9	153.3	22.5	14.4	81.7	78.9	62.9	55.9
Σ HREE	17.6	12.7	33.9	20.7	33.9	9.8	6.4	21.5	21.8	17.2	14.3

(continued on next page)

Table 2 (*continued*)

	Metagabbro							Diorite			
Sample ID	A 42	A105	A124	A96	A124	A128	AT10.4	A14	A 103	A115	A116
Parameters											
Eu/Eu*	1.7	1.4	0.8	0.9	0.8	1.1	1.2	1.1	1.0	1.0	1.2
$(La/Sm)_N$	1.1	1.3	1.9	2.4	1.9	1.0	1.1	1.7	1.7	1.8	1.9
$(Gd/Yb)_N$	1.5	1.3	1.8	2.0	1.8	1.6	1.6	1.6	1.6	1.5	1.5
Sr/Sr*	0.2	0.3	0.1	0.1	0.1	0.4	0.4	0.1	0.1	0.1	0.2

4. Intrusion-related gold mineralization in the Atud area

Gold mineralization occurred in three areas: the main Atud occurring on the eastern and northeastern slopes of Gabal Atud, Atud East-I (NE of the Atud area), and Atud East-II (SE of the Atud area) (Harraz, 1999) (Fig. 1b). The main Atud mineralization was genetically related to the metagabbro–diorite complex that was intruded by quartz veins (Fig. 1b). The mineralization was associated with a NNW–SSE brittle–ductile shear zone within hydrothermal alteration zones and quartz veins that occupy the pre-existing fractures. Furthermore, this mineralization represents a mesothermal vein-type gold mineralization style of the Arabian–Nubian Shield (Harraz, 1999, 2002).

The Atud gold mine is one of many in the Egyptian Eastern Desert that was exploited during Pharaonic times, but no ore has been produced since then (Gabra, 1986). Detailed work was done at the Atud gold mine by the Egyptian Geologic Survey and Mining Authorities (EGSMA) between 1953 and 1969, including surface and subsurface geological studies, drilling, mapping, mine workings and sampling of the altered rocks, quartz veins and country rocks (Gabra, 1986). In the main Atud mine, EGSMA performed underground prospecting and drifting on three levels along the strike of the main lode (NNW–SSE brittle–ductile shear zone) for a total length of 690 m (Fig. 5). The inclined shafts connected these levels and winzes down the dip of the lode for a total length of 230 m. The levels are about 30 m, along the dip, below one another, and four main shafts are recognized (Fig. 5). The characteristics of these levels are shown in Table 1. In addition, EGSMA excavated 135 surface trenches in the main Atud mine area. Six quartz veins were exposed on the eastern slope of Gabal Atud and 12 quartz veins were exposed on the southeastern slope. The gold content varied from <0.l to 31 g/t (average: 16.28 g/t), with 19,000 tons of rock and 348 kg of pure gold in the principal lode (Gabra, 1986). In addition, 1600 tons of dump with 12.4 g/t of gold are present in the area (Hussein and El Sharkawi, 1990). More information can be found in unpublished EGSMA reports in the Information Center.

4.1. Quartz veins

Field and optical microscopy observations suggest that there are two generations of quartz veins; the older one is grayish-to-white, mineralized trending N 30°–40° W dipping 45° toward SW. The younger vein is non-mineralized, milky-white, trending NE–SW dipping 15° toward NW (Fig. 6a–b). These veins are differentiated in the different underground levels. In the first level (42 m depth), the main quartz vein is composed of bluish or grayish quartz and is frequently associated with variable amounts of milky quartz (Fig. 6c). In the second level (72 m depth), the main quartz veins are milky quartz trending N 30°–40° W dipping 55° SW with variable amounts of bluish or grayish quartz. The quartz veins extend discontinuously up to 270 m and are nearly 70 cm-thick (Fig. 6d). Pinching, swelling and bifurcation into small veins and veinlets are observed in this level (Fig. 6e). The third level (165 m depth) contains large amounts of milky quartz with subordinate bluish or grayish quartz, directed N 40° W, and is cut by carbonate veinlets (Fig. 6f).

4.2. Ore mineralogy

The ore mineralogical studies revealed that the sulfides associated with gold mineralization include arsenopyrite, pyrite, chalcopyrite, sphalerite, and enargite with goethite as iron oxide minerals. These ore minerals occur as disseminations within the metasomatic hydrothermal alteration zones (Fig. 6g–i), as well as along the borders between the zones and the quartz veins (Fig. 6h), cutting through the altered metagabbro–diorite complex. Gangue minerals include quartz, sericite/kaolinite, carbonate (calcite, dolomite, and ankerite), and chlorite.

Arsenopyrite occurs as individual rhombic or prismatic zoned grains disseminated in the quartz veins and wall rock (Fig. 7a) and is intergrown with euhedral arsenian-pyrite (with ~2 atom% As; unpublished data) (Fig. 7b). Pyrite occurs as arsenic-bearing pyrite associated with arsenopyrite (Fig. 7c) and also occurs as disseminated subhedral or anhedral zoned grains replacing by chalcopyrite in some samples (Fig. 7d). Inclusions of sphalerite and enargite are common in the large pyrite and arsenopyrite grains, respectively (Fig. 7e–f). Goethite occurs mainly as alteration products replacing the iron-bearing sulfide minerals in the quartz veins and alteration zones (Fig. 7b–d). Gold is mostly associated with arsenopyrite, arsenic-bearing pyrite and sphalerite, with an average ~70 wt.% Au (+26 wt.% Ag) (unpublished data). Gold occurs along microfractures of arsenopyrite (Fig. 7b) and pyrite (Fig. 7g) in altered wall rocks and mineralized quartz veins. Gold also occurs either as inclusions in large pyrite crystals (Fig. 7h) or as disseminated grains with chalcopyrite and pyrite in the alteration zones (Fig. 7i).

The contact relationships of the minerals in the paragenesis revealed the three mineralization phases at the Atud Au deposit (Fig 8). The first phase is represented by disseminated euhedral pyrite and arsenopyrite, as well as quartz that are observed as large anhedral crystals. The second (main ore) phase is represented by chalcopyrite, sphalerite, and enargite, with gold enclosed as inclusions in pyrite and arsenopyrite. During this stage, small polygonal crystals of a second type of quartz were deposited, forming thin veinlest. The third phase is represented by goethite mineral occurred under the supergene condition.

4.3. Hydrothermal alteration types

The Atud gold mineralization is closely associated with intense hydrothermal alteration in the metagabbro–diorite complex along the NNW–SSE shear zones at the eastern and northeastern slopes of Gabal Atud, with typical greenschist facies alteration assemblages (Harraz, 1999, 2002.

The hydrothermal alteration is divided into three zones: Zone-1, zone-2 and zone-3 according to field, petrographic and XRD data. They occur around quartz veins and are associated with the main shear/fault zone trending NNW–SSE (Fig. 5).

Zone 1 occurs around the main mineralized quartz veins distributed in all underground levels (Fig. 5). The zone is characterized by grayish/reddish color (Fig. 9a), highly sulfidized (Fig. 9b), cut by mostly gray quartz veins (Fig. 9c) with variable amounts of milky and smoky quartz

Table 3
Major and trace elements of the median of least altered rocks and the altered rocks from alteration zones 1, 2, and 3.

	Mean	Zone 1										Zone 2			Zone 3			
Sample ID		A34	A39	A47	A49	A53	A60	A64	At68	A75	A-sh-1	A66	A67	A81	A19	A40	A58	AT10.1
SiO_2	52.05	52.57	52.24	50.21	48.71	52.37	42.10	44.44	70.67	42.99	51.86	56.58	57.85	57.85	53.21	53.62	49.13	23.42
Al_2O_3	16.11	17.39	15.36	15.43	16.48	14.00	18.40	10.78	10.82	17.53	16.30	18.64	13.71	17.51	16.36	17.46	15.21	10.18
Fe_2O_3	7.46	5.06	4.97	5.60	5.28	6.27	5.61	7.10	3.02	7.32	4.02	3.74	6.09	4.58	7.32	7.39	9.84	3.13
FeOt	6.72	4.55	4.47	5.04	4.75	5.64	5.05	6.39	2.72	6.59	3.62	3.36	5.48	4.12	6.59	6.65	8.85	2.81
MgO	6.76	2.40	3.60	3.89	3.72	3.04	3.35	6.77	1.14	3.59	3.47	1.43	1.48	1.96	4.28	4.90	3.25	4.17
CaO	8.71	4.94	6.08	6.27	6.20	5.81	8.19	7.71	1.65	6.28	7.01	3.98	4.39	4.64	7.89	3.93	5.79	32.56
Na_2O	2.81	0.22	0.31	0.84	0.20	0.25	0.25	0.12	0.10	0.54	0.61	3.78	2.40	3.27	3.25	5.10	2.23	0.91
K2O	0.83	4.56	3.83	3.53	4.22	3.63	4.44	2.75	2.54	4.50	3.67	3.03	2.56	2.52	0.59	0.28	2.09	0.14
TiO_2	0.82	0.83	0.66	0.65	0.65	1.03	0.63	0.61	0.37	1.13	0.59	0.42	0.82	0.59	0.81	1.01	1.82	0.18
P_2O_5	0.20	0.20	0.12	0.13	0.11	0.10	0.08	0.11	0.07	0.14	0.06	0.23	0.22	0.15	0.21	0.20	0.17	0.00
MnO	0.13	0.08	0.09	0.09	0.09	0.11	0.12	0.15	0.03	0.13	0.09	0.07	0.08	0.06	0.13	0.09	0.12	0.05
LOI	3.79	10.67	11.75	13.06	12.90	12.10	14.16	17.78	6.34	14.01	12.29	8.09	8.91	6.87	5.93	4.49	8.75	24.69
Trace elements (ppm)																		
Ag	0.8	7.0	1.3	0.7	2.2	10.0	14.0	1.2	69.6	29.4	0.9	0.9	12.3	2.4	0.7	1.2	3.4	1.0
As	10.6	810.7	91.1	3040.2	2522.3	1969.5	1404.0	294.4	4220.0	2697.4	211.0	158.0	1194.5	172.0	6.0	6450.4	4093.9	48.5
Au (ppb)	46.4	275.1	25.0	156.3	237.8	182.6	270.6	28.0	790.2	184.2	159.6	118.6	176.1	48.6	53.9	74.7	90.3	155.4
Ba	113.9	375.2	440.4	131.2	185.6	273.7	25.0	72.0	9.0	259.2	211.0	334.0	188.1	245.0	144.0	80.9	347.9	73.8
C	2340.6	27,056.0	19,785.0	25,364.0	14,553.0	4882.4	30,903.0	13,295.0	5717.3	24,749.0	25,541.0	12,529.0	26,180.0	12,589.0	7687.8	44,681.0	23,086.0	52,887.0
Co	35.0	13.0	20.7	20.7	16.0	19.1	16.0	25.8	36.0	21.8	13.0	5.0	11.2	31.0	27.0	22.1	22.0	26.2
Cu	29.2	27.9	19.1	6.0	15.6	44.6	46.5	6.3	83.8	35.3	27.2	112.6	118.2	39.6	19.9	32.7	79.0	0.2
Ga	31.1	25.4	22.4	16.8	17.2	20.8	38.4	11.1	20.4	22.1	33.1	52.7	16.4	40.5	33.6	20.7	25.6	9.7
Hf	2.5	0.6	0.8	1.1	0.8	1.0	1.5	0.6	1.0	1.1	1.3	1.5	2.7	1.4	0.9	3.0	1.7	0.4
Ni	150.5	19.4	52.3	25.8	21.0	24.9	360.9	32.5	398.3	25.1	408.9	157.6	6.8	163.4	206.5	47.3	11.2	55.6
Pb	12.7	9.4	7.6	9.3	10.9	10.8	4.0	10.6	23.4	12.8	1.6	5.3	9.2	5.5	35.7	10.3	14.6	22.0
S	331.1	36,168.0	20,741.0	20,427.0	33,425.0	5986.8	26,186.0	16,316.0	21,224.0	1091.8	6015.9	9123.3	16,301.0	1989.2	70.7	5525.8	28,274.0	823.0
Sb	3.5	8.6	26.4	20.0	9.8	21.7	30.4	3.8	143.1	37.6	13.6	7.0	17.5	10.3	14.4	3.9	3.6	0.4
Sn	1.8	1.4	1.2	1.3	0.9	1.3	2.3	1.0	1.6	1.4	2.5	1.9	0.8	1.7	2.0	2.5	2.0	0.5
Sr	363.1	106.5	145.6	114.6	133.8	133.5	131.7	132.5	32.1	142.3	203.7	169.9	88.5	110.6	375.7	197.9	160.4	276.7
V	446.8	113.0	137.0	132.0	124.0	156.0	357.0	142.0	258.2	167.0	264.2	214.7	66.0	275.1	344.3	179.0	337.0	
Y	32.1	10.0	7.5	9.9	8.6	12.6	14.7	8.2	8.0	10.7	12.9	20.1	15.0	18.9	32.1	19.2	21.2	5.2
Zn	108.1	25.3	53.2	72.2	77.3	123.4	82.9	97.0	100.1	79.0	90.8	85.8	24.7	97.5	216.4	65.5	119.3	11.3
Zr	105.0	184.0	74.0	76.0	68.0	90.0	96.0	67.0	74.0	98.0	70.0	163.0	167.0	100.0	90.0	124.0	137.0	15.0
Density (g/cm^3)	2.91	2.85	2.88	2.89	2.91	2.88	2.90	3.00	2.79	2.92	2.87	2.87	2.85	2.86	2.88	2.90	2.97	2.84
Ishikawa AI	39.71	57.43	53.76	51.07	55.37	52.40	47.98	54.87	67.79	54.26	48.38	36.47	37.30	36.14	30.44	36.45	39.97	11.40

veins (Fig. 9d), and is affected by faulting (N30W/80SW) (Fig. 9a). Based on the petrographic and XRD studies, the samples of this zone are composed mainly of sericite and muscovite with quartz and pyrite and minor amounts of ankerite, dolomite, albite, and graphite (Figs. 9e–f and 10a–b). Mineralogical studies revealed large amounts of pyrite and arsenopyrite with the alteration minerals (Fig. 6g).

Zone 2 represents the outer halo of zone 1 (Fig. 5) and is cut by a milky quartz vein and calcite veinlets (Figs. 9g and 6i). The zone is characterized by a large amount of quartz, albite, and sericite/kaolinite with pyrite, dolomite, clinochlore, and muscovite (Figs. 9h–i and 10c). Zone 2 is rich in pyrite (Fig. 6i).

Zone 3 occurs along the outer contact of zone 2 (Fig. 5) and is represented by rocks enriched in carbonate (dolomite and ankerite) and chlorite along with arsenopyrite (Fig. 6h). The zone consists of ankerite, calcite, dolomite, chlorite, chamosite (XRD results), chlinochlore, and albite, with minor amounts of muscovite and quartz (Figs. 9j–l and 10d).

5. Geochemical characteristics

The metagabbro–diorite complex, which includes the Atud gold mineralization, was divided into least-altered and altered rocks. Ten representative samples were collected from the least-altered metagabbro–diorite complex, including 6 samples of metagabbros and 4 samples of dioritic rocks. In addition, 18 representative samples were collected from the different alteration zones. Each sample was analyzed for major, trace, and rare earth elements (Tables 2 and 3).

5.1. Geochemistry of the least-altered metagabbro–diorite complex

Geochemical classification using the $Na_2O + K_2O$ versus SiO_2 diagram (Fig. 11a) suggested by Cox et al. (1979) in Wilson (1989) shows that metagabbros are in fields of gabbro and gabbro/diorite, whereas diorites fall in the diorite and gabbro/diorite fields. These rocks have calc-alkaline affinities (Fig. 11b), and are equivalent to calc-alkaline basalt (CAB) (Fig. 11c). The relationship between Ni and FeO^*/MgO content was used by Miyashiro and Shido (1975) to differentiate volcanic rocks according to different tectonic settings, whereas the plots of the analyzed metagabbro–diorite complex mostly fall in the island arc field (Fig. 11d). Pearce and Norry (1979) suggested that Zr/Y ratios increase from mid-ocean ridges to within plate basalts due to heterogeneities of the source, whereas the low Zr and Zr/Y ratio of volcanic arc basalts result from a high degree of partial melting of a depleted source. On the other hand, the high Zr and similar Zr/Y ratio of basalts are due to open-system fractional crystallization. Floyd (1993) stated that amphibole and clinopyroxene fractionation significantly increase the abundance of Zr, whereas olivine and plagioclase fractionation

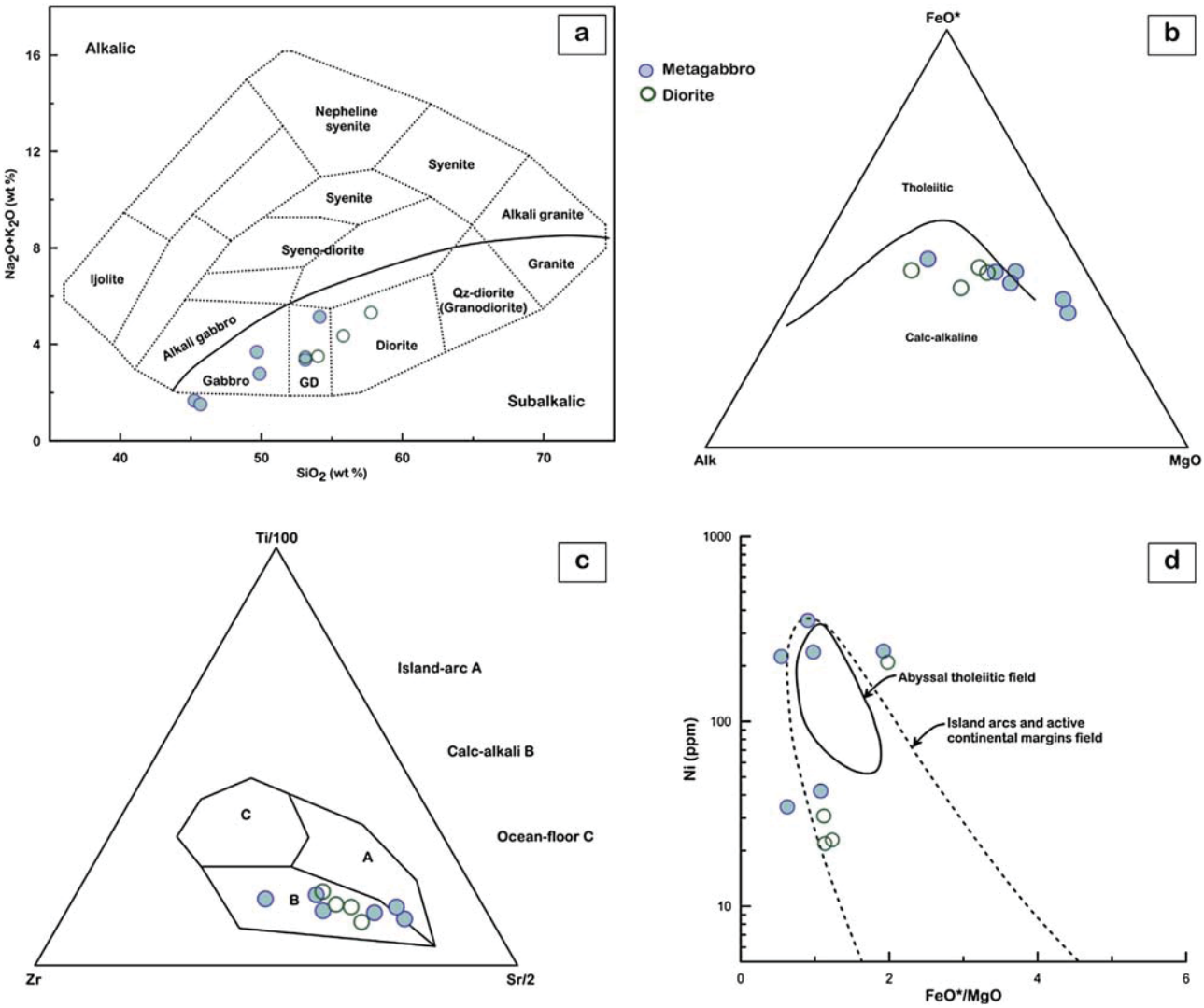

Fig. 11. Geochemical diagrams of metagabbro–diorite diagrams: a) TAS diagram after Cox et al. (1979). The dividing line between alkalic and subalkalic after Miyashiro (1978); b) AFM ternary diagram after Irvine and Baragar (1971); c) Ti/100–Zr–Sr/2 ternary diagram after Pearce and Cann (1973); d) FeO*/MgO–Ni diagram after Miyashiro and Shido (1975).

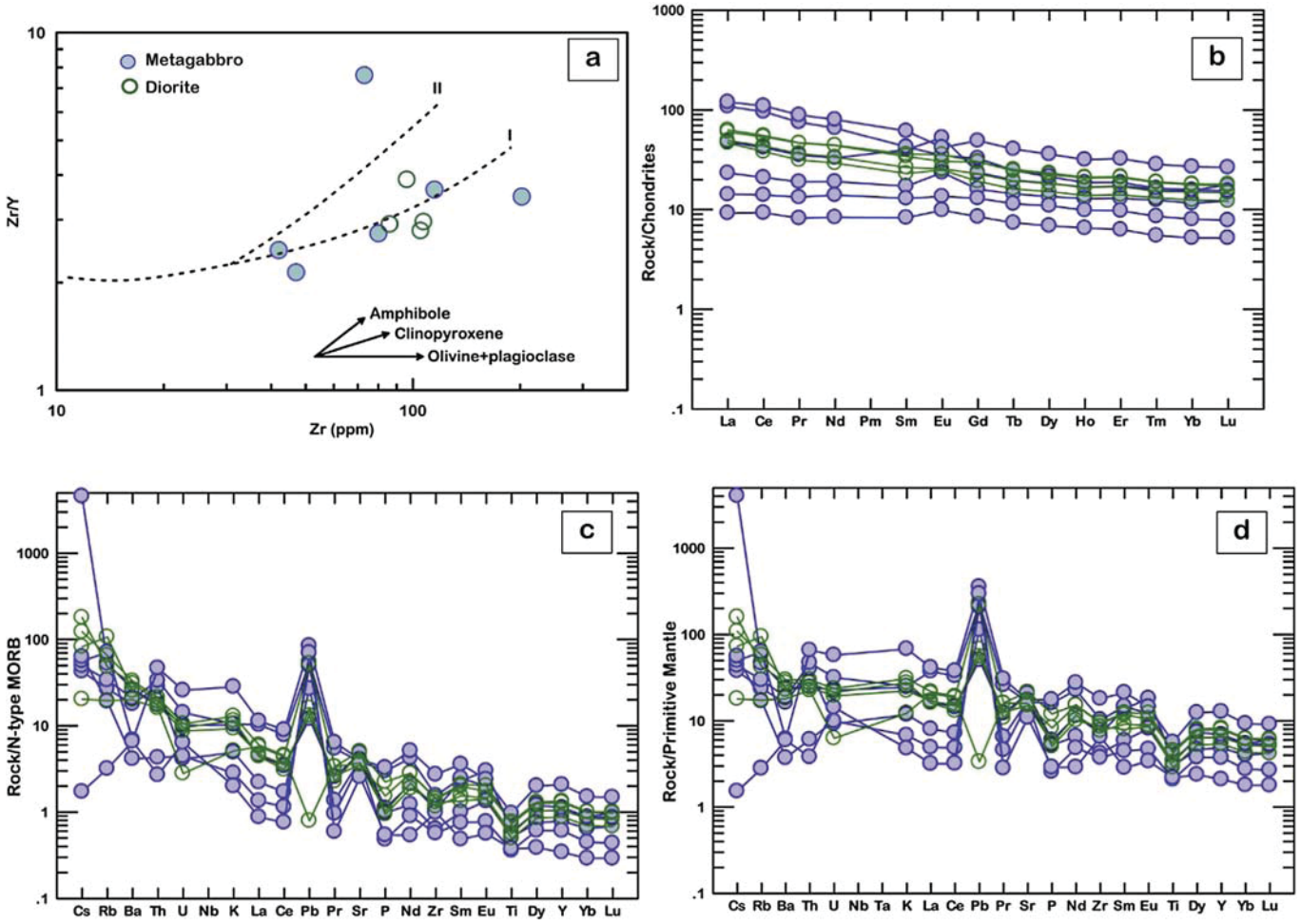

Fig. 12. Geochemical diagrams of metagabbro–diorite diagrams: a) Zr/Y–Zr binary diagram, vectors for fractional crystallization after Floyd (1993) and melting curves I and II after Drury et al. (1983); b) Chondrite-normalized REE patterns (Sun and McDonough, 1989); c) N-type MORB-normalized patterns (Sun and McDonough, 1989); d) Primitive mantle-normalized trace element patterns (Sun and McDonough, 1989).

does not change the Zr/Y ratio. Based on a Zr versus Zr/Y binary diagram, a significant variation of Zr/Y ratios increase with increasing Zr (Fig. 12a); their trend closely follows curve I of Drury et al. (1983), indicating fractional crystallization of mafic phases with or without feldspars (Drury et al., 1983). The metagabbro samples reflect clinopyroxene fractionation crystallized from mafic phases from island arcs (Drury et al., 1983), whereas the metadiorite samples reflect amphibole fractionation crystallized from mafic phases from Andean-type arcs (Drury et al., 1983) and are typical of calc-alkaline volcanic arc lavas (Brown et al., 1977). The chondrite-, N-type MORB, and primitive mantle-normalized REE patterns of metagabbro–diorite complex rocks are characterized by concave profiles (Fig. 12b–d). These patterns are characterized by an enriched LREE, with an average 81.8 for metagabbro and 69.9 for dioritic rocks [$(La/Sm)_N = 1.1–2.4$ for metagabbro and 1.7–2.0 for dioritic rocks], and a practically flat HREE, with an average 19.3 for metagabbro and 18.7 for dioritic rocks [average $(Gd/Yb)_N = 1.6$

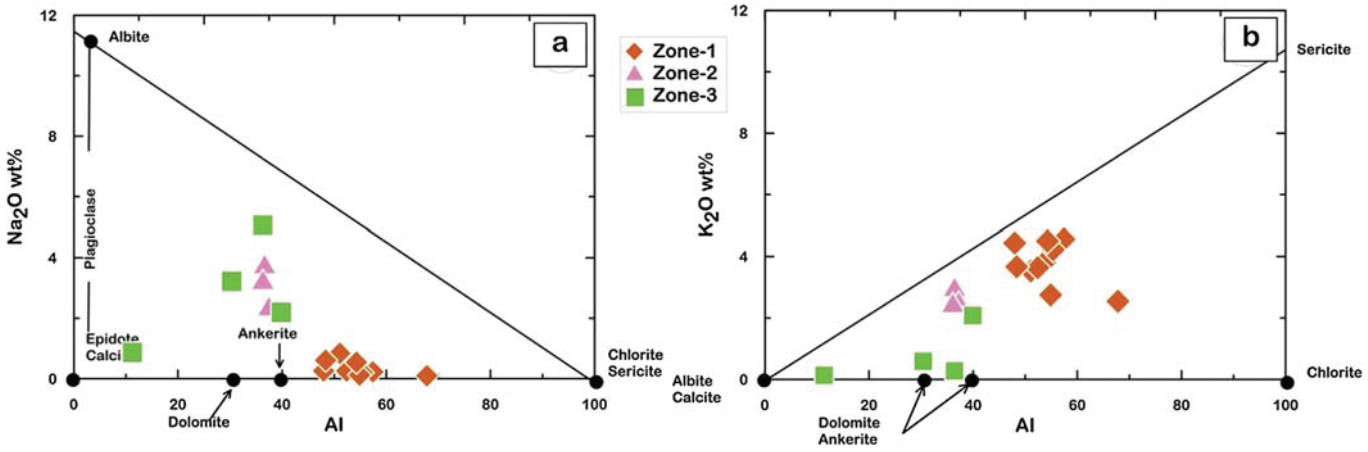

Fig. 13. Relationship between alteration index (Al) and (a) Na_2O and (b) K_2O for the altered rocks (Large et al., 2001).

and 1.5 for metagabbro and dioritic rocks, respectively]. The patterns also show slight positive Eu anomalies ($Eu/Eu^* = 0.8–1.7$ and 1.0–1.2 for metagabbro and dioritic rocks, respectively). The positive Eu anomalies are due to plagioclase accumulations that contributed to Eu and light REE abundances, and led to a dilution of the HREE (Hassanipak et al., 1996). In addition, the Sr/Sr* is used as a comparison with the Eu contents, and positive Eu/Eu* and Sr/Sr* anomalies of analyzed rocks refer to plagioclase accumulations (Nagihara and Casey, 2001) (Fig. 12c–d).

5.2. Alteration geochemistry

The geochemical characteristics of the hydrothermally altered wall rocks associated with the Atud gold deposit are based on a number of whole-rock geochemical analyses of the samples from the underground levels of the alteration zones (Table 3). The major factor responsible for the precipitation of different ores is the chemical interaction between the rocks and the circulating hydrothermal solutions (Rose and Burt, 1979 and Susak, 1994). When the hydrothermally altered wall rocks were compared to the least-altered rocks, a higher K_2O content was observed, indicating that sericite, kaolinite, muscovite and chlorite are the main alteration phases in all the alteration zones, with higher loss on ignition (LOI) content referring to more intense alteration. Generally, these altered wall rocks have a large proportion of sulfur representing arsenopyrite and pyrite. Furthermore the model percentages of the arsenopyrite, chalcopyrite, and enargite are changed in the three alteration zones. Zone 1 and 2 which have no enragite contain 5–8 vol.% and 3–5 vol.% arsenopyrite, and 2–3 vol.% and 1–2 vol.% chalcopyrite, respectively. On the other hand zone 3 has high amount of arsenopyrite (5–8 vol.%) with enargite (1–2 vol.%). Some elements, e.g. Au, Ag, S, and Sb with As, are most common in alteration zone 1 decreasing outward to zone 3. In zone 2, a high amount of SiO_2 reflects silicification, whereas in zone 3, a significant amount of CaO and C with Na_2O indicates carbonatization and albitization. In addition, the relationship between Na_2O and K_2O in the Ishikawa alteration index ($AI = [100(K_2O + MgO) / (K_2O + MgO + CaO + Na_2O)]$) of Ishikawa et al. (1976) for altered rocks suggests sericite in zone 1 with some chlorite and carbonate, dolomite/ankerite in zones 2 and 3, and albite/calcite in zone 3 (Fig. 13a–b).

5.2.1. Mass balance calculation

During hydrothermal alteration processes, the mass changes of each alteration zone are respected to the unaltered precursor and elemental compositions that experience gains/losses or dilutions are set from the composition-volume comparison of altered and unaltered rocks (Gresens, 1967). The Gresens' equation was improved by Grant (1986, 2005) who suggested that the immobile elements plot along an isocon line that has no mass transfer during alteration processes. GEOISO-Windows (Coelho, 2006) is a recent version of software which determines and plots mass balance/volume changes during alteration processes. The absolute mobility of different elements, which indicates the mass balance/volume change, is defined using Gresens (1967) equations and a best-fit isocon line (Grant, 1986) and requires selection of immobile elements. This enables the determination of mass gains/losses of mobile elements in altered rocks. Al, Ti, and Zr represent high field strength elements and are assumed to be immobile elements (or their mobility is not significant during alteration processes). Furthermore, aluminum is considered to be an immobile element within greenschist-grade metamorphic conditions under low-to-moderate temperature hydrothermal systems (Barton et al., 1991). Based on mass/volume gains and losses, each of the alteration zones has different additions and depletions of major/trace elements (Tables 3 and 4). On

Table 4
Elements/oxides mass changes in relation to original whole rock mass ((Mfi − Moi) / Mo) and in relation to original elements/oxides mass in original rock ((Mfi − Moi) / Moi) (data resulted from GEOISO—A Windows™ program).

	Zone 1		Zone 2		Zone 3	
	(Mfi − Moi)/Mo	(Mfi − Moi) / Moi	(Mfi − Moi) / Mo	(Mfi − Moi) / Moi	(Mfi − Moi) / Mo	(Mfi − Moi) / Moi
SiO_2	1.636	0.031	3.618	0.07	−3.241	−0.062
Al_2O_3	0	0	0	0	0	0
Fe_2O_3	−1.724	−0.231	−2.807	−0.376	0.073	0.01
FeO^t	−1.565	−0.233	−2.533	−0.377	0.061	0.009
MgO	−3.063	−0.453	−5.19	−0.768	−2.243	−0.332
CaO	−2.361	−0.271	−4.503	−0.517	4.94	0.567
Na_2O	−2.451	−0.872	0.243	0.087	0.314	0.112
K_2O	3.153	3.798	1.787	2.153	0.019	0.023
TiO_2	−0.07	−0.085	−0.229	−0.279	0.225	0.274
P_2O_5	−0.084	−0.419	−0.006	−0.031	−0.037	−0.184
MnO	−0.024	−0.187	−0.062	−0.478	−0.021	−0.163
LOI	9.425	2.487	3.926	1.036	8.151	2.151
Ag	13.559	16.141	4.21	5.012	0.88	1.047
As	1812.758	170.372	481.917	45.293	2873.594	270.075
Au	197.514	4.252	64.488	1.388	55.402	1.193
Ba	95.528	0.839	133.974	1.177	62.077	0.545
C	17,925.864	7.659	14,234.031	6.081	32,584.856	13.922
Co	−13.66	−0.39	−19.753	−0.564	−8.526	−0.244
Cu	3.751	0.128	58.154	1.99	6.626	0.227
Ga	−7.107	−0.228	4.259	0.137	−6.757	−0.217
Hf	−1.455	−0.587	−0.648	−0.261	−0.847	−0.342
Ni	−5.89	−0.039	−44.593	−0.296	−63.255	−0.42
Pb	−2.063	−0.163	−6.224	−0.491	9.809	0.774
S	19,484.857	58.844	8526.297	25.749	9109.961	27.512
Sb	29.726	8.397	7.704	2.176	2.545	0.719
Sn	−0.216	−0.121	−0.355	−0.199	0.137	0.076
Sr	−228.211	−0.629	−243.834	−0.672	−88.036	−0.242
V	−251.304	−0.562	−267.195	−0.598	−134.648	−0.301
Y	−21.179	−0.66	−14.622	−0.456	−10.92	−0.341
Zn	−23.461	−0.217	−40.907	−0.378	4.148	0.038
Zr	−10.242	−0.098	33.932	0.323	−5.401	−0.051

(Mfi − Moi) / Mo: Mass change in relation to original rock mass.
(Mfi − Moi) / Moi: Mass change in relation to original element mass.

the x–y plots of least-altered vs. altered samples (calculated using GEOISO-Windows), Al_2O_3 is shown to be an immobile element in all alteration zones during hydrothermal alteration (Fig. 14a–c). The mass balance calculations and isocon diagrams reveal that the samples from zone 1 are enriched in K_2O, SiO_2, and LOI with Au, Ag, As, Ba, C, Cu, S, and Sb (Figs. 14a and 15a–b). Mass change (MC) and volume change

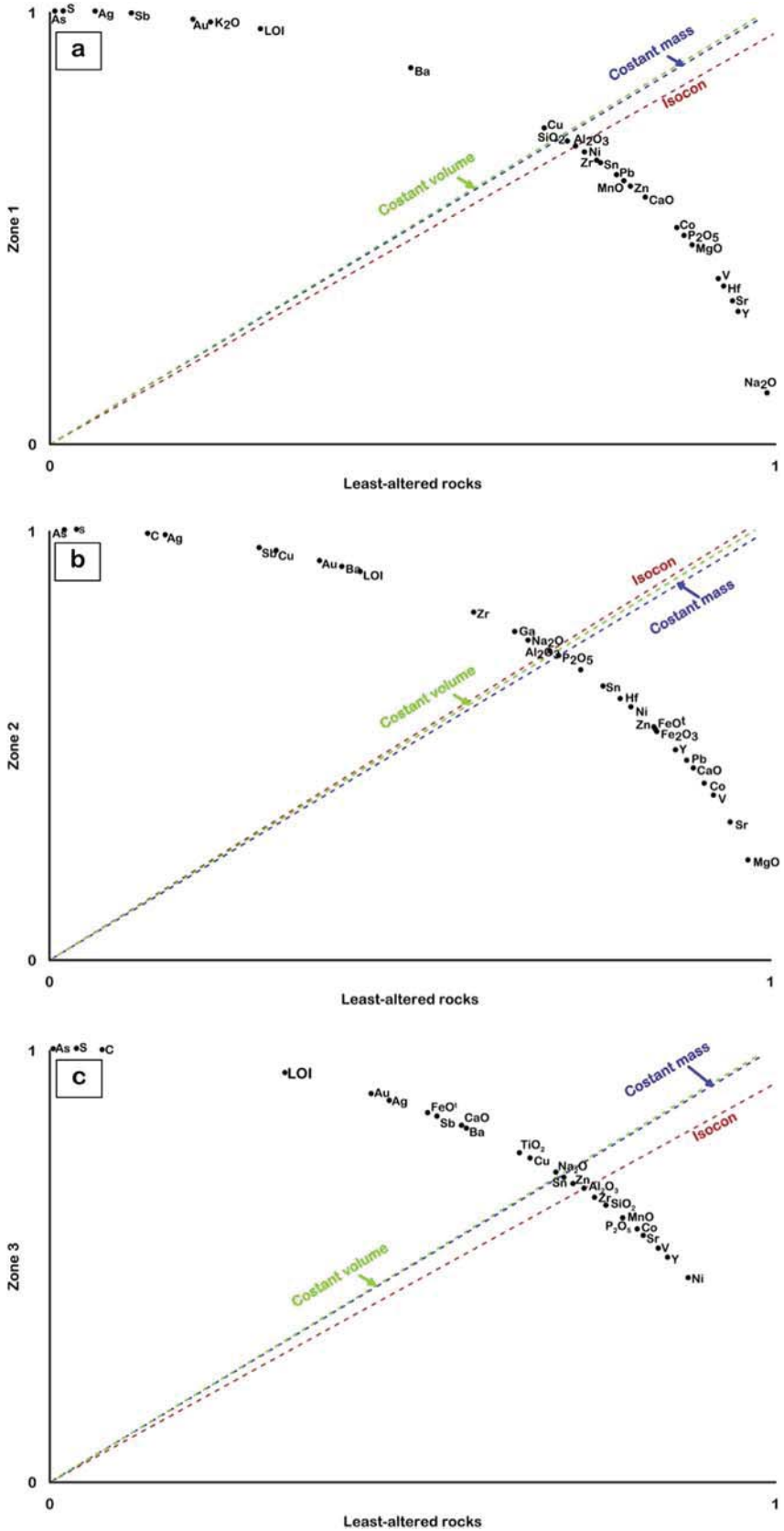

Fig. 14. Isocon diagram comparing the mean composition of least-altered samples and altered samples from (a) zone 1; (b) zone 2; and (c) zone 3.

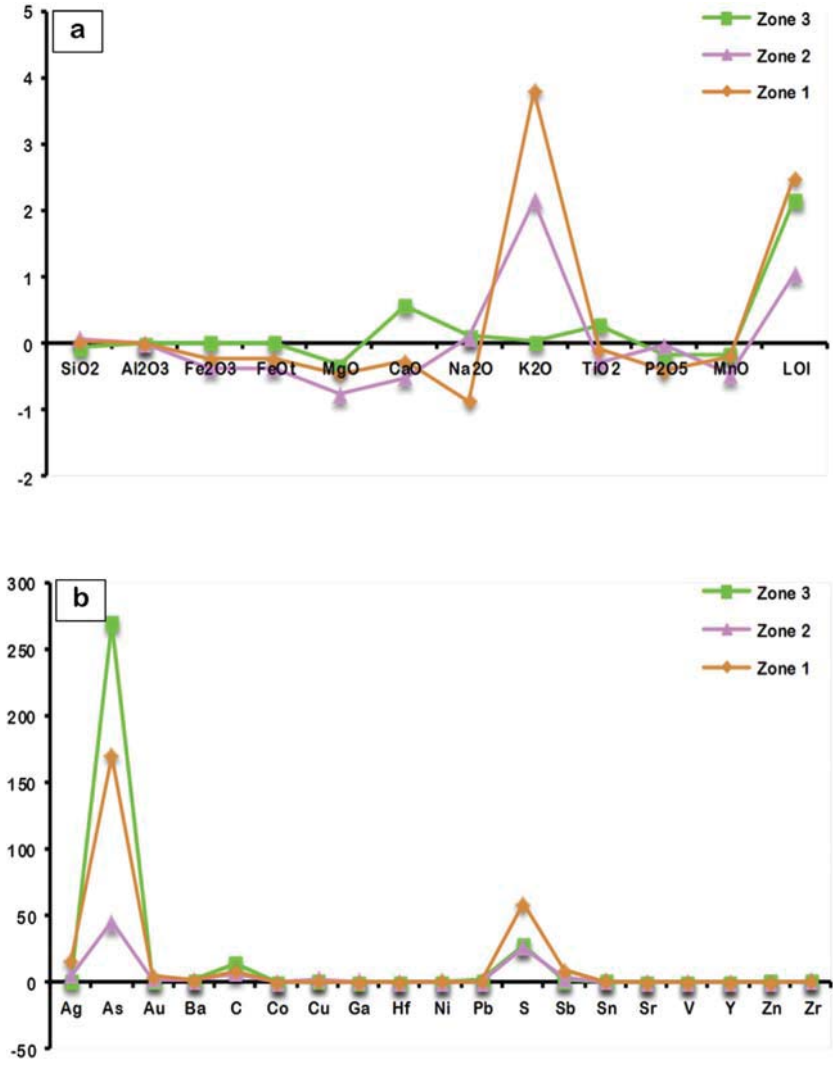

Fig. 15. Gain/loss of major oxides (wt.%) and trace elements (ppm) during alteration in the different zones of hydrothermal alteration based on mean data of the least altered samples as a reference for calculations, a) for zone 1; b) for zone 2, and (c) for zone 3.

(VC) of this zone are calculated as 5.6% and 6.4%, respectively (Table 5). Enrichment of K_2O, Na_2O, and SiO_2 with higher Au, Ag, As, Ba, C, Cu, Ga, S, Sb, and Zr is observed in samples from zone 2 (Figs. 14b and 15a–b), with −3.1% MC and −1.4% VC (Table 5). Finally, common additions of CaO, Fe_2O_3, K_2O, Na_2O, TiO_2 and LOI with significant Au, Ag, As, Ba, C, Cu, Pb, S, Sb, Sn, and Zn enrichments characterize the chemical changes in the altered rocks in zone 3 (Fig. 14c and 15a–b) with 8.8% MC and 9.2% VC (Table 5). Zone 3 has the highest amount of MC and VC, because it is rich in iron and titanium which they easily leached from the least altered metagabbro–diorite rocks and concentrated in this zone.

6. Chemistry of alteration minerals

The alteration minerals, e.g. sericite, carbonate, chlorite, and albite (Fig. 16a), were analyzed with an electron microprobe. These minerals are distributed in the alteration zones associated with ore minerals and associated with gold mineralization in the underground levels.

Table 5
Whole rock mass and volume change in different zones of alteration at Atud gold mine area.

	Zone 1	Zone 2	Zone 3
MC: whole rock mass change	5.639	−3.069	8.851
VC: Whole rock volume change	6.37	−1.374	9.227

Sericite is a very fine-grained white mica of white and yellowish color, and typically forms by the decomposition of feldspars. Sericite is the main secondary and alteration mineral observed in the gold-bearing hydrothermal alteration zone 1 and in mineralized quartz veins. Sericite is associated with kaolinite, muscovite, quartz, and pyrite. Electron microprobe data of sericite (Table 6) showed that its muscovite component was high in all analyzed flakes (average $X_{Ms} = 0.89$) and that its phengite content ($Mg + Fe_{a.p.f.u.}$) varied from 0.10 to 0.55 and 0.13 to 0.29 in wall rocks and mineralized veins, respectively. A negative correlation between ($Si + Mg + Fe^{2+}$) and ($Al^{iv} + Al^{vi}$) for sericite minerals (Fig. 16b) indicates that their chemical compositional variations are controlled by phengitic substitutions of Si for Al ($Fe^{(VI)}$, $Mg^{(VI)} + Si^{(IV)} + Al^{(VI)} + Al^{(IV)}$) (Muscovite formula calculated by Monier and Robert, 1986 and Tindle and Webb, 1990).

Carbonate minerals represent the second component of the secondary minerals, after sericite. Carbonate minerals occur either as thin veinlets traversing the silicified and chloritized wall rocks in alteration zones 2 and 3 or as disseminated grains intermingling with the mineralized quartz veins and wall rocks (Fig. 9l). The electron microprobe data indicate that these carbonate minerals have higher amounts of $CaCO_3$ and lower amounts of $MgCO_3$ and $FeCO_3$ in the quartz veins than in the wall rocks (Table 7). Furthermore, in alteration zones 2 and 3, carbonate

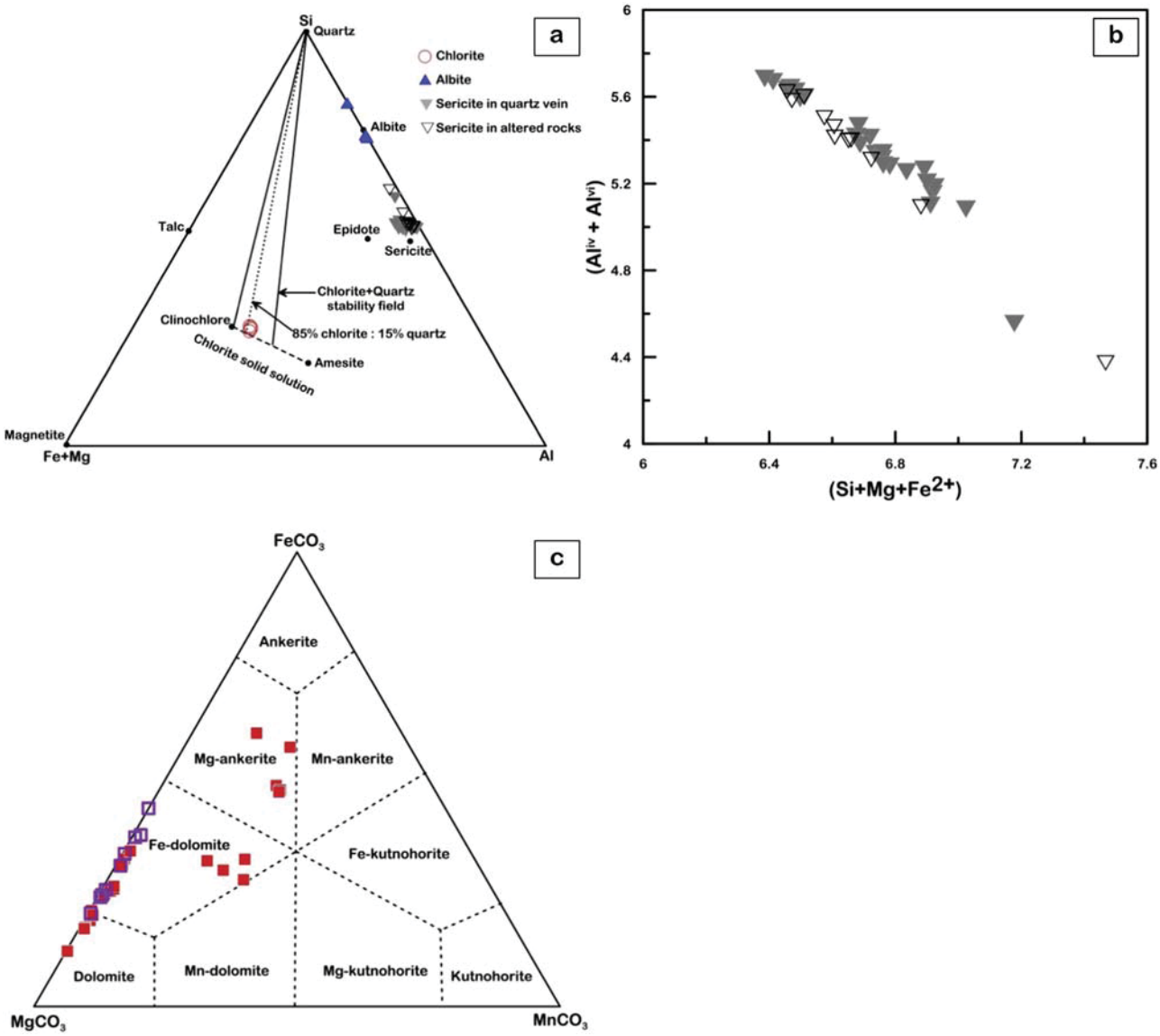

Fig. 16. a) Si–Al– (Fe + Mg) cation ternary diagram showing representative composition of different secondary and hydrothermal minerals from Atud gold mine (after Kranidiotis and MacLean, 1987); b) (Si + Mg + Fe^{2+}) versus (Al^{iv} + Al^{vi}) of the sericite minerals from the mineralized quartz vein and altered wall rocks; c) $FeCO_3$–$MgCO_3$–$MnCO_3$ triangular classification diagram of Trdlička and Hoffman (1976) showing compositions of carbonate of the dolomite–ankerite series in samples of the mineralized veins and altered rocks.

minerals occur principally as dolomite, iron-dolomite and magnesium-ankerite, whereas in quartz veins the carbonate minerals differentiated into iron-dolomite (Fig. 16c).

Chlorite occurs as colorless-to-olive green flakes associated with disseminated arsenopyrite in hydrothermal alteration zone 3. Electron microprobe data of chlorite flakes (Table 8) revealed that they are generally iron-rich (FeO^t 20.64–20.10 wt.%) and are composed of pycnochlorite or ripidolite ($Al^{(iv)}$ = 2.30–2.36 pfu and 2.41–2.51 pfu, respectively) (Fig. 17a). The estimated formation temperatures are 289–295 °C and 301–312 °C for pycnochlorite and ripidolite, respectively, and were calculated using the empirical Si–Aliv substitution geothermometer of Cathelineau (1988).

Albite represents the main secondary feldspar produced by plagioclase substitution, and is found disseminated in altered wall rocks with chlorite in alteration zone 2. The representative chemical compositions of albite show high SiO_2 (68.2–79.5 wt.%), Al_2O_3 (14.2–19.9 wt.%), and Na_2O (7.3–11.9 wt.%) content and low amounts of CaO (0.1–0.2 wt.%) (Table 9). Albite was relatively pure having a high Ab content in all analyzed samples (Ab = 95.08%–99.20%). The triangular diagram of albite (Ab), anorthite (An) and orthoclase (Or) end-members refers to the analyzed samples plotted in the albite field (Fig. 17b).

7. Discussions and conclusions

In the Atud area, the metagabbro–diorite complex occurred in Gabal Atud in the central part of the Egyptian Eastern Desert. The complex is intruded into serpentinites and their derivatives and metatuffs, and is later intruded by younger olivine gabbro norite. The Atud gold mineralization is considered as a vein-type gold deposit closely associated with intense hydrothermal alteration haloes along the NW–SE brittle–ductile shear zone. It was genetically related to the metagabbro–diorite complex that was intruded by quartz veins that occupied the pre-existing fractures. These quartz veins that are linked to the shear zone system are younger than the intrusion of olivine gabbro norite, having two generations: a mineralized grayish-to-white old vein (trending N 30°–40° W), and a younger, non-mineralized milky white vein (trending NE–SW). Underground levels were drifting along the NNW–SSE brittle–ductile shear zone that represents the strike of the main lode. The

Table 6
Representative electron microprobe data of sericite from the alteration zones and quartz veins in the Atud gold mine area.

Sericite from altered rocks											
Spot no.	3/1.	6/1.	7/1.	9/1.	10/1.	11/1.	12/1.	13/1.	16/1.	18/1.	19/1.
SiO_2	47.44	46.69	48.95	47.86	49.28	47.29	48.69	55.29	48.65	48.23	47.79
TiO_2	0.13	0.15	0.19	0.17	0.02	0.06	0.08	0.08	0.05	0.13	0.10
Al_2O_3	34.13	33.54	31.75	33.53	37.19	35.79	36.41	28.27	34.72	34.96	35.14
FeO	0.55	0.29	0.47	0.50	0.24	0.33	0.27	0.33	0.40	0.32	0.37
MnO	0.02	0.02	0.00	0.00	0.01	0.06	0.01	0.00	0.00	0.00	0.00
MgO	1.13	0.87	0.80	1.16	0.55	0.97	0.54	0.87	0.95	0.88	0.91
CaO	0.13	0.08	0.10	0.08	0.03	0.05	0.16	0.06	0.11	0.04	0.05
Na2O	0.33	0.36	0.35	0.47	2.09	0.61	1.66	0.32	0.31	0.36	0.32
K2O	9.03	8.84	8.14	8.76	6.13	8.17	6.65	7.58	9.01	8.50	8.76
SrO	0.00	0.03	0.00	0.01	0.00	0.00	0.00	0.00	0.00	0.00	0.00
BaO	0.00	0.04	0.06	0.08	0.04	0.09	0.06	0.06	0.07	0.06	0.00
F	0.00	0.00	0.00	0.00	0.00	0.01	0.01	0.02	0.00	0.00	0.00
Cl	0.02	0.02	0.02	0.00	0.01	0.00	0.00	0.01	0.03	0.01	0.01
Cr_2O_3	0.00	0.01	0.00	0.04	0.03	0.02	0.05	0.02	0.00	0.00	0.01
H2O*	4.46	4.37	4.40	4.46	4.67	4.51	4.60	4.55	4.54	4.52	4.51
Total	97.36	95.31	95.22	97.12	100.29	97.96	99.19	97.45	98.83	98.01	97.97
Number of cations on basis of 24 (O, OH, F, Cl)											
Si	6.37	6.40	6.67	6.44	6.33	6.28	6.34	7.26	6.42	6.40	6.35
Al ^{iv}	1.63	1.60	1.33	1.56	1.67	1.72	1.66	0.74	1.58	1.60	1.65
Al ^{vi}	3.77	3.81	3.76	3.75	3.95	3.88	3.92	3.64	3.82	3.86	3.86
Al total	5.40	5.42	5.10	5.31	5.63	5.60	5.59	4.38	5.40	5.47	5.51
Ti	0.01	0.02	0.02	0.02	0.00	0.01	0.01	0.01	0.00	0.01	0.01
Cr	0.00	0.00	0.00	0.00	0.00	0.00	0.01	0.00	0.00	0.00	0.00
Fe	0.06	0.03	0.05	0.06	0.03	0.04	0.03	0.04	0.04	0.04	0.04
Mn	0.00	0.00	0.00	0.00	0.00	0.01	0.00	0.00	0.00	0.00	0.00
Mg	0.23	0.18	0.16	0.23	0.11	0.19	0.10	0.17	0.19	0.17	0.18
Ca	0.02	0.01	0.01	0.01	0.00	0.01	0.02	0.01	0.02	0.01	0.01
Na	0.09	0.10	0.09	0.12	0.52	0.16	0.42	0.08	0.08	0.09	0.08
K	1.55	1.54	1.41	1.50	1.00	1.38	1.10	1.27	1.52	1.44	1.49
Ba	0.00	0.00	0.00	0.00	0.00	0.00	0.00	0.00	0.00	0.00	0.00
OH*	4.00	4.00	4.00	4.00	4.00	4.00	4.00	3.99	3.99	4.00	4.00
Fe/Fe + Mg	0.21	0.16	0.25	0.19	0.20	0.16	0.22	0.18	0.19	0.17	0.19
X_{MS}	0.95	0.94	0.94	0.92	0.66	0.90	0.72	0.94	0.95	0.94	0.95
Fe + Mg	0.29	0.21	0.22	0.29	0.13	0.23	0.13	0.21	0.23	0.21	0.22
Fe + Mg + Si	6.66	6.61	6.88	6.72	6.46	6.51	6.47	7.47	6.65	6.61	6.57

	Sericite from quartz veins																							
Spot no.	1/1.	2/1.	6/1.	7/1.	9/1.	10/1.	11/1.	14/1.	15/1.	16/1.	17/1.	18/1.	19/1.	21/1.	23/1.	27/1.	28/1.	29/1.	30/1.	16/1.	17/1.	19/1.	20/1.	27/1.	28/1.
SiO_2	49.06	48.68	48.11	49.18	48.36	49.17	49.58	47.44	47.84	47.97	47.65	47.90	46.79	47.77	48.47	49.01	47.28	47.99	47.91	47.84	55.07	48.30	47.40	46.10	47.28
TiO_2	0.07	0.14	0.07	0.07	0.08	0.10	0.09	0.41	0.07	0.13	0.23	0.33	0.09	0.18	0.13	0.44	0.27	0.22	0.28	0.16	0.06	0.05	0.21	0.42	0.15
Al_2O_3	37.39	33.11	36.38	37.21	37.11	37.12	37.07	34.26	34.61	34.75	33.59	34.90	34.62	32.97	34.09	32.75	33.36	34.68	33.65	33.98	30.46	36.35	32.76	32.78	31.62
FeO	0.28	1.36	1.00	0.54	0.17	0.26	0.46	1.51	0.85	1.15	1.13	1.27	1.25	1.66	0.60	1.44	1.75	1.13	1.41	1.27	0.33	0.27	1.70	1.83	2.22
MnO	0.01	0.00	0.01	0.00	0.01	0.01	0.00	0.02	0.00	0.00	0.03	0.00	0.00	0.00	0.00	0.00	0.04	0.01	0.01	0.02	0.00	0.00	0.01	0.00	0.01
MgO	0.37	1.73	0.62	0.43	0.43	0.52	0.55	1.52	1.15	1.29	1.52	1.18	1.38	1.84	1.43	1.41	1.83	1.27	1.68	1.20	0.83	0.57	1.58	1.21	1.59
CaO	0.06	0.05	0.02	0.05	0.05	0.07	0.14	0.00	0.06	0.05	0.08	0.04	0.08	0.04	0.03	0.03	0.00	0.02	0.01	0.08	0.10	0.05	0.04	0.02	0.00
Na2O	2.00	0.27	0.23	1.48	1.42	1.85	1.69	0.26	0.22	0.21	0.18	0.24	0.23	0.13	0.09	0.23	0.32	0.27	0.17	0.30	3.94	0.46	0.34	0.31	0.25
K2O	6.02	10.01	9.07	6.38	6.94	5.88	6.26	9.91	9.32	8.99	9.95	9.11	9.15	10.04	9.67	9.60	8.83	9.93	9.87	8.87	6.11	7.77	9.19	9.77	9.54
SrO	0.00	0.00	0.00	0.00	0.00	0.00	0.00	0.05	0.00	0.00	0.00	0.01	0.00	0.00	0.00	0.00	0.04	0.05	0.00	0.00	0.00	0.00	0.00	0.00	0.00
BaO	0.14	0.17	0.01	0.10	0.12	0.10	0.00	0.29	0.06	0.12	0.17	0.26	0.17	0.11	0.01	0.55	0.29	0.03	0.18	0.18	0.00	0.10	0.29	0.38	0.18
F	0.00	0.00	0.00	0.00	0.00	0.00	0.00	0.01	0.00	0.00	0.00	0.00	0.00	0.00	0.00	0.00	0.00	0.00	0.00	0.00	0.00	0.00	0.00	0.00	0.00
Cl	0.01	0.00	0.00	0.01	0.00	0.00	0.01	0.00	0.00	0.01	0.00	0.00	0.01	0.02	0.01	0.00	0.01	0.02	0.01	0.01	0.01	0.01	0.00	0.01	0.01
Cr_2O_3	0.00	0.01	0.04	0.06	0.14	0.07	0.09	0.10	0.02	0.00	0.03	0.11	0.00	0.04	0.01	0.03	0.04	0.05	0.07	0.00	0.00	0.04	0.00	0.01	0.00
H2O*	4.66	4.54	4.59	4.66	4.61	4.66	4.68	4.53	4.52	4.54	4.50	4.56	4.47	4.49	4.53	4.54	4.48	4.55	4.52	4.49	4.72	4.56	4.45	4.38	4.39
Total	100.07	100.07	100.15	100.17	99.44	99.81	100.62	100.31	98.72	99.20	99.06	99.91	98.24	99.28	99.07	100.03	98.53	100.22	99.77	98.40	101.63	98.53	97.97	97.22	97.24
Number of cations on basis of 24 (O, OH, F, Cl)																									
Si	6.31	6.43	6.28	6.33	6.28	6.33	6.34	6.27	6.35	6.34	6.35	6.30	6.27	6.37	6.41	6.48	6.33	6.31	6.35	6.38	6.99	6.34	6.39	6.31	6.45
Al ^{iv}	1.69	1.57	1.72	1.67	1.72	1.67	1.66	1.73	1.65	1.66	1.65	1.70	1.73	1.63	1.59	1.52	1.67	1.69	1.65	1.62	1.01	1.66	1.61	1.69	1.55
Al ^{vi}	3.98	3.58	3.88	3.97	3.97	3.96	3.94	3.61	3.77	3.75	3.63	3.72	3.73	3.56	3.72	3.57	3.60	3.69	3.60	3.72	3.54	3.97	3.60	3.59	3.53
Al total	5.67	5.15	5.60	5.64	5.68	5.63	5.59	5.34	5.42	5.41	5.28	5.41	5.47	5.18	5.31	5.10	5.27	5.38	5.25	5.34	4.55	5.63	5.21	5.29	5.08
Ti	0.01	0.01	0.01	0.01	0.01	0.01	0.01	0.04	0.01	0.01	0.02	0.03	0.01	0.02	0.01	0.04	0.03	0.02	0.03	0.02	0.01	0.00	0.02	0.04	0.02
Cr	0.00	0.00	0.00	0.01	0.01	0.01	0.01	0.01	0.00	0.00	0.00	0.01	0.00	0.00	0.00	0.00	0.00	0.01	0.01	0.00	0.00	0.00	0.00	0.00	0.00
Fe	0.03	0.15	0.11	0.06	0.02	0.03	0.05	0.17	0.09	0.13	0.13	0.14	0.14	0.19	0.07	0.16	0.20	0.12	0.16	0.14	0.04	0.03	0.19	0.21	0.25
Mn	0.00	0.00	0.00	0.00	0.00	0.00	0.00	0.00	0.00	0.00	0.00	0.00	0.00	0.00	0.00	0.00	0.00	0.00	0.00	0.00	0.00	0.00	0.00	0.00	0.00
Mg	0.07	0.34	0.12	0.08	0.08	0.10	0.10	0.30	0.23	0.25	0.30	0.23	0.28	0.37	0.28	0.28	0.37	0.25	0.33	0.24	0.16	0.11	0.32	0.25	0.32
Ca	0.01	0.01	0.00	0.01	0.01	0.01	0.02	0.00	0.01	0.01	0.01	0.01	0.01	0.01	0.00	0.00	0.00	0.00	0.00	0.01	0.01	0.01	0.01	0.00	0.00
Na	0.50	0.07	0.06	0.37	0.36	0.46	0.42	0.07	0.06	0.05	0.05	0.06	0.06	0.03	0.02	0.06	0.08	0.07	0.04	0.08	0.97	0.12	0.09	0.08	0.07
K	0.99	1.69	1.51	1.05	1.15	0.97	1.02	1.67	1.58	1.52	1.69	1.53	1.56	1.71	1.63	1.62	1.51	1.67	1.67	1.51	0.99	1.30	1.58	1.70	1.66
Ba	0.01	0.01	0.00	0.01	0.01	0.01	0.00	0.02	0.00	0.01	0.01	0.01	0.01	0.01	0.00	0.03	0.02	0.00	0.01	0.01	0.00	0.01	0.02	0.02	0.01
OH*	4.00	4.00	4.00	4.00	4.00	4.00	4.00	4.00	4.00	4.00	4.00	4.00	4.00	4.00	4.00	4.00	4.00	4.00	4.00	4.00	4.00	4.00	4.00	4.00	4.00
Fe/Fe + Mg	0.30	0.31	0.48	0.41	0.18	0.22	0.32	0.36	0.29	0.33	0.29	0.38	0.34	0.34	0.19	0.36	0.35	0.33	0.32	0.37	0.18	0.21	0.38	0.46	0.44
X_{MS}	0.66	0.96	0.96	0.74	0.76	0.68	0.71	0.96	0.97	0.97	0.97	0.96	0.96	0.98	0.99	0.96	0.95	0.96	0.97	0.95	0.50	0.92	0.95	0.95	0.96
Fe + Mg	0.10	0.49	0.23	0.14	0.10	0.13	0.15	0.47	0.32	0.38	0.43	0.37	0.42	0.55	0.35	0.44	0.56	0.37	0.49	0.38	0.19	0.14	0.51	0.46	0.58
Fe + Mg + Si	6.41	6.92	6.51	6.47	6.39	6.46	6.50	6.74	6.67	6.72	6.78	6.68	6.68	6.92	6.76	6.91	6.89	6.69	6.84	6.76	7.18	6.48	6.90	6.76	7.02

Table 7
Representative electron microprobe data of carbonate from the alteration zones and quartz veins in the Atud gold mine area.

	Carbonate from alteration zones							
Spot no.	1/1.	2/1.	4/1.	5/1.	8/1.	14/1.	15/1.	17/1.	20/1.
CaO	29.78	24.51	24.53	20.02	27.76	22.07	26.29	25.06	27.69
MgO	14.25	9.37	16.64	12.12	12.69	19.51	13.08	13.98	14.21
MnO	0.37	0.51	0.39	0.01	0.42	0.32	0.25	0.22	0.31
FeO	11.31	13.25	22.72	21.35	13.15	11.50	9.50	16.22	10.60
BaO	0.04	0.00	0.03	0.01	0.06	0.00	0.00	0.00	0.00
Structural formulae basis on cation per 2 oxygens									
Ca	0.97	0.98	0.72	0.72	0.95	0.70	0.96	0.84	0.94
Mg	0.76	0.62	0.80	0.72	0.72	1.03	0.79	0.77	0.79
Mn	0.01	0.01	0.01	0.00	0.01	0.01	0.01	0.01	0.01
Fe	0.26	0.38	0.48	0.55	0.32	0.26	0.25	0.39	0.26
Ba	0.00	0.00	0.00	0.00	0.00	0.00	0.00	0.00	0.00
C	2.00	2.00	2.00	2.00	2.00	2.00	2.00	2.00	2.00
O	6.00	6.00	6.00	6.00	6.00	6.00	6.00	6.00	6.00
% molecule									
$CaCO_3$	48.29	49.18	35.78	36.18	47.50	35.19	47.93	41.83	46.97
$MgCO_3$	38.09	30.99	40.01	36.11	35.80	51.28	39.31	38.47	39.74
$MnCO_3$	0.44	0.75	0.41	0.01	0.52	0.37	0.33	0.27	0.38
$FeCO_3$	13.16	19.08	23.78	27.69	16.15	13.16	12.43	19.43	12.90
$BaCO_3$	0.02	0.00	0.01	0.01	0.03	0.00	0.00	0.00	0.00

	Carbonate from quartz veins																							
Spot no.	3/1.	4/1.	5/1.	8/1.	12/1	13/1.	20/1.	22/1.	24/1.	25/1.	26/1.	6/1.	7/1.	8/1.	9/1.	10/1.	21/1.	22/1.	23/1.	24/1.	25/1.	26/1.	29/1.	30/1.	31/1.
CaO	28.46	29.43	29.61	30.91	29.62	28.63	29.61	29.62	29.66	31.19	28.87	57.58	59.05	0.32	62.63	60.76	30.91	52.58	62.27	63.35	31.93	31.02	48.32	31.85	30.95
MgO	12.66	11.65	15.42	15.61	15.68	14.98	15.79	16.11	16.20	18.12	14.43	0.79	0.47	0.01	0.49	0.59	12.45	0.35	0.44	0.50	12.27	11.17	0.08	11.87	10.99
MnO	0.41	0.49	0.16	0.41	0.48	0.50	0.51	0.43	0.44	0.11	0.44	0.59	0.58	0.01	0.62	0.57	0.70	0.58	0.78	0.87	0.86	0.45	0.16	0.74	0.40
FeO	14.19	14.20	9.53	7.57	8.49	8.17	9.27	7.92	7.80	5.81	11.05	1.14	0.80	0.05	0.68	0.83	10.00	1.32	1.64	1.82	10.16	11.91	0.46	10.08	11.58
BaO	0.02	0.00	0.00	0.03	0.00	0.03	0.00	0.00	0.02	0.00	0.01	0.00	0.00	0.00	0.00	0.05	0.02	0.00	0.01	0.07	0.03	0.00	0.02	0.00	0.00
Structural formulae basis on cation per 2 oxygens																									
Ca	0.95	0.99	0.96	0.99	0.96	0.96	0.95	0.95	0.95	0.96	0.95	1.92	1.94	1.69	1.95	1.94	1.05	1.93	1.92	1.92	1.06	1.06	1.98	1.08	1.07
Mg	0.70	0.65	0.82	0.83	0.84	0.83	0.83	0.85	0.86	0.91	0.78	0.04	0.03	0.09	0.03	0.03	0.69	0.02	0.02	0.02	0.67	0.63	0.01	0.66	0.63
Mn	0.01	0.01	0.00	0.01	0.01	0.01	0.01	0.01	0.01	0.00	0.01	0.01	0.01	0.04	0.01	0.01	0.02	0.02	0.02	0.02	0.02	0.01	0.00	0.02	0.01
Fe	0.34	0.34	0.22	0.17	0.20	0.20	0.21	0.18	0.18	0.13	0.26	0.03	0.02	0.19	0.02	0.02	0.24	0.03	0.04	0.04	0.24	0.29	0.01	0.24	0.29
Ba	0.00	0.00	0.00	0.00	0.00	0.00	0.00	0.00	0.00	0.00	0.00	0.00	0.00	0.00	0.00	0.00	0.00	0.00	0.00	0.00	0.00	0.00	0.00	0.00	0.00
C	2.00	2.00	2.00	2.00	2.00	2.00	2.00	2.00	2.00	2.00	2.00	2.00	2.00	2.00	2.00	2.00	2.00	2.00	2.00	2.00	2.00	2.00	2.00	2.00	2.00
O	6.00	6.00	6.00	6.00	6.00	6.00	6.00	6.00	6.00	6.00	6.00	6.00	6.00	6.00	6.00	6.00	6.00	6.00	6.00	6.00	6.00	6.00	6.00	6.00	6.00
% molecule																									
$CaCO_3$	47.58	49.73	47.77	49.55	47.84	48.07	47.25	47.64	47.61	47.76	47.40	95.76	97.09	84.28	97.28	96.82	52.28	96.43	96.18	95.79	53.14	53.20	98.80	53.81	53.67
$MgCO_3$	34.89	32.45	41.01	41.25	41.75	41.46	41.54	42.71	42.87	45.74	39.05	2.17	1.27	4.34	1.25	1.55	34.71	1.06	1.12	1.25	33.67	31.58	0.27	33.06	31.42
$MnCO_3$	0.50	0.60	0.19	0.48	0.57	0.61	0.59	0.50	0.52	0.12	0.53	0.72	0.70	1.92	0.70	0.66	0.86	0.78	0.88	0.96	1.04	0.56	0.24	0.91	0.51
$FeCO_3$	17.02	17.22	11.03	8.71	9.84	9.84	10.62	9.14	8.99	6.38	13.02	1.36	0.94	9.45	0.76	0.95	12.14	1.74	1.82	1.97	12.14	14.66	0.68	12.22	14.41
$BaCO_3$	0.01	0.00	0.00	0.01	0.00	0.01	0.00	0.00	0.01	0.00	0.00	0.00	0.00	0.00	0.00	0.02	0.01	0.00	0.00	0.03	0.01	0.00	0.01	0.00	0.00

Table 8
Representative electron microprobe data of chlorite from the alteration zones in the Atud gold mine area.

Spot no	3/1	4/1	5/1	11/1
SiO_2	27.67	27.37	27.00	26.42
TiO_2	0.04	0.02	0.10	0.05
Al_2O_3	19.64	19.99	20.10	20.04
FeO	20.44	20.79	20.35	21.71
MnO	0.28	0.25	0.23	0.25
MgO	18.89	18.67	18.96	18.53
CaO	0.03	0.03	0.03	0.08
Na_2O		0.02	0.01	0.05
K_2O				
Cl				0.01
F		0.01		
TOTAL	86.34	86.50	86.13	86.49
O = F,Cl	0.00	0.00	0.00	0.00
T2	12.40	12.41	12.44	12.51
Cations based on 28 anions (O, F), anhydrous basis				
Si	5.71	5.65	5.59	5.50
Ti	0.01	0.00	0.02	0.01
$Al^{(iv)}$	2.29	2.35	2.41	2.50
$Al^{(vi)}$	2.49	2.52	2.50	2.42
Al	4.78	4.86	4.91	4.92
Fe^2	3.53	3.59	3.52	3.78
Mn	0.05	0.04	0.04	0.04
Mg	5.81	5.75	5.85	5.75
Ca	0.01	0.01	0.01	0.02
Na	0.00	0.01	0.00	0.02
K	0.00	0.00	0.00	0.00
Cl	0.00	0.00	0.00	0.00
F	0.00	0.01	0.00	0.00
Fe/(Fe + Mg)	0.38	0.38	0.38	0.40
$Al^{iv}c$	2.29	2.35	2.41	2.50
T(°C)	288.57	295.40	301.17	312.30

Table 9
Representative electron microprobe data of albite from the alteration zones in the Atud gold mine area.

Spot no.	1/1	12/1	13/1	14/1	18/1
SiO_2	68.95	69.02	69.31	68.22	79.49
Al_2O_3	19.49	19.50	19.88	19.96	14.20
FeO	0.03	0.08	0.04	0.10	0.09
CaO	0.24	0.11	0.10	0.16	0.11
Na_2O	11.87	11.57	11.73	11.98	7.28
K_2O	0.05	0.05	0.07	0.06	0.48
BaO	0.06	0.03	0.04		
Total	100.69	100.36	101.17	100.48	101.65
Formula					
Si	2.99	3.00	2.99	2.97	3.32
Al	1.00	1.00	1.01	1.02	0.70
Fe^2	0.00	0.00	0.00	0.00	0.00
Ca	0.01	0.01	0.00	0.01	0.00
Na	1.00	0.98	0.98	1.01	0.59
K	0.00	0.00	0.00	0.00	0.03
Ba	0.00	0.00	0.00	0.00	0.00
T2	2.61	2.61	2.59	2.62	2.51
Anorthite	1.10	0.52	0.47	0.73	0.79
Albite	98.62	99.20	99.14	98.94	95.08
Orthoclase	0.27	0.28	0.39	0.33	4.12

geological, petrographical and XRD analytical studies suggest that there are three main hydrothermal alteration zones of mineral assemblages with gradual boundaries placed around mineralized and non-mineralized quartz veins in these levels. Zone 1 is a zone of sericite/kaolinite, muscovite, quartz, and pyrite with minor amounts of graphite, ankerite, dolomite, and/or albite. Larger amounts of quartz, albite, and sericite/kaolinite are found in zone 2 with minor amounts of pyrite, dolomite, clinochlore, and muscovite. Zone 3 is characterized by significant amounts of carbonate (ankerite/calcite) and chlorite (chamosite/chlinochlore) with albite and arsenopyrite and lower amounts of pyrite, muscovite, and quartz. The ore mineralogy includes mainly arsenopyrite and pyrite, with minor amounts of chalcopyrite, sphalerite, and enargite with goethite, associated with gold mineralization that occurred along the contact of quartz veins with hydrothermal alteration zones as well as within these zones. The first, second (main ore), and third (supergene) phases of mineralization represent the contact relationships of gold with sulfide and gangue minerals in the paragenesis. The geochemical behavior of the least-altered metagabbro–diorite complex rocks reveals that the metagabbros are calc-alkaline gabbro and gabbro/diorite, whereas the diorites are calc-alkaline diorite and gabbro/diorite. These rocks are equivalent to calc-alkaline basalt (CAB) formed in island arc environments indicating clinopyroxene fractionation for metagabbros and amphibole fractionation for dioritic rocks.

GEOISO-Windows calculated the mass/volume gain and loss values, with Al_2O_3 considered as an immobile element. The mass balance calculations and isocon diagrams concluded that K_2O, Au, S, and Sb decrease from alteration zone 1 to zone 2, indicating that gold mineralization is highly related to sericitic, kaolinitic and muscovite alteration. Zone 3, which has a high amount of CaO, Fe_2O_3, and Na_2O with K_2O – indicating

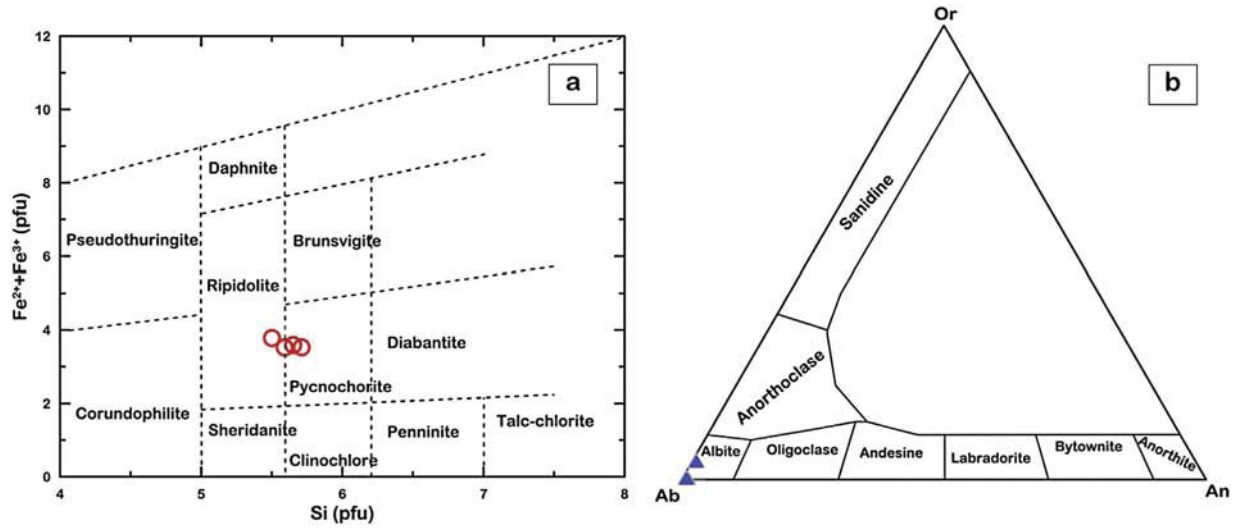

Fig. 17. a) Si versus ($Fe^{2+} + Fe^{3+}$) diagram showing chlorite composition in the alteration zone in the Atud gold mine (classification of Hey (1954)); b) feldspars chemistry in the Or–Ab–An diagram of Deer et al. (1992) (Ab: albite; Or: orthoclase; An: anorthite).

carbonatization, chloritization and albitization – is characterized by a lower amount of gold. Therefore, gold decreases from zone 1 outwards to zone 3.

Sericite exhibited a high muscovite component in all analyzed flakes (average $X_{Ms} = 0.89$) and a phengite content ranging from 0.10 to 0.55 and 0.13 to 0.29 in wall rocks and mineralized veins, respectively. Carbonate has higher amounts of calcite ($CaCO_3$) and lower amounts of $MgCO_3$ and $FeCO_3$ in wall rocks than in quartz veins. Chlorite flakes are generally iron-rich (FeO^t 20.64–20.10 wt.%) and are composed of pycnochlorite and ripidolite, with $Al^{(iv)} = 2.30–2.36$ pfu and 2.41–2.51 pfu, respectively and estimated formation temperatures of 289–295 °C and 301–312 °C, respectively. Albite is accompanied with chlorite but was generally pure in all samples (Ab = 95.08%–99.20%).

Acknowledgments

This study builds on the PhD thesis of the first author in the frame of a scholarship offered from the Egyptian Government (Cultural Affairs and Mission Sector) in cooperation with the Turkish Government (YTB, Turkey). The authors are grateful to Prof. B. Zoheir (Benha Univ. Egypt), Dr. M. Afife (Benha Univ. Egypt), and Mr. L. Gumus (ITU, Turkey) for the help during the field workings. We also thank the help of the group of Geochemistry Research Laboratories (ITU/JAL, Turkey) during the laboratory works. Also, great thanks go to Prof. B. Zoheir (Benha Univ. Egypt) for doing the electron microprobe work during a short-term visit to the Technical University of Clausthal as well as to Prof. Dr. B. Lehmann (TU-Clausthal, Germany) for allowing the analytical facilities. Additionally the authors are much more grateful to Prof. Franco Pirajno (Editor-in-Chief) and the anonymous reviewers for their constructive comments, corrections and helpful suggestions which greatly improved the manuscript.

References

Abdel-Rahman, A.F.M., Doig, R., 1987. The Rb–Sr geochronological evolution of the Ras Gharib segment of the northern Nubian Shield. J. Geol. Soc. 144 (4), 577–586.
Barton, M.D., Staude, J.M., Snow, E.A., Johnson, D.A., 1991. Aureole systematics. Rev. Mineral. Geochem. 26 (1), 723–847.
Brown, L.D., Reilinger, R.E., Holdahl, S.R., Balazs, E.I., 1977. Postseismic crustal uplift near Anchorage, Alaska. J. Geophys. Res. 82 (23), 3369–3378.
Carr, M., 2007. Igpet 2007 for Windows XP or Vista. Terra Softa Inc.
Cathelineau, M., 1988. Cation site occupancy in chlorites and illites as function of temperature. Clay Miner. 23 (4), 471–485.
Coelho, J., 2006. GEOISO—a Windows™ program to calculate and plot mass balances and volume changes occurring in a wide variety of geologic processes. Comput. Geosci. 32 (9), 1523–1528.
Cox, K.G., Bell, J.D., Pankhurst, R.J., 1979. The interpretation of igneous rocks. George Allen & Unwin.
Deer, W.A., Howie, R.A., Zussman, J., 1992. An introduction to the rock-forming minerals. 696. Longman, London.
Drury, S.A., Holt, R.W., van Calsteren, P.C., Beckinsale, R.D., 1983. Sm–Nd and Rb–Sr ages for Archaean rocks from western Karnataka. J. Geol. Soc. India 24, 454–459.
El-Gaby, S., List, F.K., Tehrani, R., 1988. Geology, evolution and metallogenesis of the Pan-African Belt in Egypt. The Pan-African Belt of Northeast Africa and Adjacent Areas, pp. 17–68.
El-Taher, A., Kratz, K.L., Nossair, A., Azzam, A.H., 2003. Determination of gold in two Egyptian gold ores using instrumental neutron activation analysis. Radiat. Phys. Chem. 68 (5), 751–755.
Floyd, P.A., 1993. Geochemical discrimination and petrogenesis of alkalic basalt sequences in part of the Ankara melange, central Turkey. J. Geol. Soc. 150 (3), 541–550.
Gabra, S., 1986. Gold in Egypt: a commodity package, minerals, petroleum and groundwater assessment program: USAID project 363-0105. Geol. Surv. Egypt.
Ghoneim, M.F., 1989. Mineral chemistry of some gabbroic rocks of the Central Eastern Desert, Egypt. J. Afr. Earth Sci. 9 (2), 289–295.
Grant, J.A., 1986. The isocon diagram; a simple solution to Gresens' equation for metasomatic alteration. Econ. Geol. 81 (8), 1976–1982.
Grant, J.A., 2005. Isocon analysis: a brief review of the method and applications. Phys. Chem. Earth, Parts A/B/C 30 (17), 997–1004.
Gresens, R.L., 1967. Composition–volume relationships of metasomatism. Chem. Geol. 2, 47–65.
Harraz, H.Z., 1999. Wall rock alteration, Atud gold mine, Eastern Desert, Egypt: processes and P–T–XCO_2 conditions of metasomatism. J. Afr. Earth Sci. 28 (3), 527–551.
Harraz, H.Z., 2002. Fluid inclusions in the mesozonal gold deposit at Atud mine, Eastern Desert, Egypt. J. Afr. Earth Sci. 35 (3), 347–363.
Harraz, H.Z., Ashmawy, M.H., 1994. Structural and lithogeochemical constraints on the localization of gold deposits at the El Sid-Fawa khir gold mine area, Eastern Desert, Egypt. Egypt. J. Geol. 38, 629–648.
Hashad, A.H., 2013. Present status of geochronological data on the Egyptian basement complex. Evolution and Mineralization of the Arabian–Nubian Shield. 1, pp. 31–46.
Hassanipak, A.A., Ghazi, A.M., Wampler, J.M., 1996. Rare earth element characteristics and K–Ar ages of the Band Ziarat ophiolite complex, southeastern Iran. Can. J. Earth Sci. 33 (11), 1534–1542.
Hey, M.H., 1954. A new review of the chlorites. Mineral. Mag. 30, 277–292.
Hussein, A.A., El Sharkawi, M.A., 1990. Mineral Deposits. The Geology of Egypt. Balkema, Rotterdam, pp. 511–566.
Irvine, T., Baragar, W., 1971. A guide to the chemical classification of the common volcanic rocks. Can. J. Earth Sci. 8 (5), 523–548.
Ishikawa, Y., Sawaguchi, T., Iwaya, S., Horiuchi, M., 1976. Delineation of prospecting targets for Kuroko deposits based on modes of volcanism of underlying dacite and alteration halos. Min. Geol. 26, 105–117.
Klemm, D., Klemm, R., Murr, A., 2001. Gold of the pharaohs—6000 years of gold mining in Egypt and Nubia. J. Afr. Earth Sci. 33 (3), 643–659.
Kranidiotis, P., MacLean, W.H., 1987. Systematics of chlorite alteration at the Phelps Dodge massive sulfide deposit, Matagami, Quebec. Econ. Geol. 82 (7), 1898–1911.
Large, R.R., Gemmell, J.B., Paulick, H., Huston, D.L., 2001. The alteration box plot: a simple approach to understanding the relationship between alteration mineralogy and lithogeochemistry associated with volcanic-hosted massive sulfide deposits. Econ. Geol. 96 (5), 957–971.
Leitch, C.H.B., Lentz, D.R., 1994. The Gresens approach to mass balance constraints of alteration systems: methods, pitfalls, examples. Alteration and Alteration Processes Associated With Ore-forming systems: Geological Association of Canada, Short Course Notes. 11, pp. 161–192.
Lindgren, W., 1894. Characteristic features of California gold-quartz veins. Geol. Soc. Am. Bull. 6 (1), 221–240.
Meyer, C., Hemley, J.J., 1967. Wall rock alteration. Geochemistry of hydrothermal ore deposits 1, p. 166.
Middelburg, J.J., van der Weijden, C.H., Woittiez, J.R., 1988. Chemical processes affecting the mobility of major, minor and trace elements during weathering of granitic rocks. Chem. Geol. 68 (3), 253–273.
Miyashiro, A., 1978. Nature of alkalic volcanic rock series. Contrib. Mineral. Petrol. 66 (1), 91–104.
Miyashiro, A., Shido, F., 1975. Tholeiitic and calc-alkalic series in relation to the behaviors of titanium, vanadium, chromium, and nickel. Am. J. Sci. 275 (3), 265–277.
Monier, G., Robert, J.L., 1986. Muscovite solid solutions in the system K_2O–MgO–FeO–Al_2O_3–SiO_2–H_2O: an experimental study at 2 kbar PH_2O and comparison with natural Li-free white micas. Mineral. Mag. 50, 257–266.
Nagihara, S.S., Casey, J.F., 2001. Whole-rock geochemistry of amphibolites and metagabbros from the West Iberia Margin, Leg 173. In: Beslier, M.-O., Whitmarsh, R.B., Wallace, P.J., Girardeau, J. (Eds.), Proc. ODP, Sci. Results, p. 173.
Pearce, J.A., Cann, J.R., 1973. Tectonic setting of basic volcanic rocks determined using trace element analyses. Earth Planet. Sci. Lett. 19 (2), 290–300.
Pearce, J.A., Norry, M.J., 1979. Petrogenetic implications of Ti, Zr, Y, and Nb variations in volcanic rocks. Contrib. Mineral. Petrol. 69 (1), 33–47.
Pirajno, F., 2009. Hydrothermal Processes Associated With Meteorite Impacts. Springer, Netherlands, pp. 1097–1130.
Pohl, W., 1988. Precambrian Metallogeny of Northeast-Africa. In: El-Gaby, S., Greiling, R.O. (Eds.), The Pan-African Belt of Northeast Africa and Adjacent Areas. Friedrich Vieweg und Sohn, Braunschweig/Wiesbaden, pp. 319–341.
Reed, M.H., 1997. Hydrothermal alteration and its relationship to ore fluid composition. Geochemistry of hydrothermal ore deposits 3, pp. 303–365.
Rose, A.W., Burt, D.M., 1979. Hydrothermal alteration. In: Barnes, H.L. (Ed.), Geochemistry of hydrothermal ore deposits, third ed. John Wiley & Sons, New York, pp. 173–227.
Sabet, A.H., Bordonosov, V.P., 1984. The gold ore formations in the Eastern Desert of Egypt. Ann. Geol. Surv. Egypt 16, 35–42.
Streckeisen, A., 1976. To each plutonic rock its proper name. Earth Sci. Rev. 12 (1), 1–33.
Sun, S.S., McDonough, W.F., 1989. Chemical and isotopic systematics of oceanic basalts: implications for mantle composition and processes. Geol. Soc. Lond., Spec. Publ. 42 (1), 313–345.
Susak, N.J., 1994. In: Lenz, D.R. (Ed.), Alteration Factors Affecting Ore Deposition, pp. 115–130.
Tindle, A.G., Webb, P.C., 1990. Estimation of lithium contents in trioctahedral micas using microprobe data: application to micas from granitic rocks. Eur. J. Mineral. 595–610.
Trdlička, Z., Hoffman, V., 1976. Untersuchungen der chemischen Zusammensetzung der Gangkarbonate von Kutná Hora (ČSSR). Freiberger Forschungshefte C 321, pp. 29–81.
Vail, J.R., 1988. Tectonics and evolution of the Proterozoic basement of NE Africa. The Pan-African belts of NE Africa and Adjacent areas. Friedr Vieweg and Sohn, pp. 185–226.
Wilson, M., 1989. Igneous Petrogenesis: A Global Tectonic Approach. p. 466.